Subcontractor Report

Processing of CuInSe$_2$-Based Solar Cells: Characterization of Deposition Processes in Terms of Chemical Reaction Analyses

Phase II Annual Report
6 May 1996 — 5 May 1997

T. Anderson
Department of Chemical Engineering
University of Florida
Gainesville, Florida

NREL

National Renewable Energy Laboratory

Processing of CuInSe$_2$-Based Solar Cells: Characterization of Deposition Processes in Terms of Chemical Reaction Analyses

Phase II Annual Report
6 May 1996 — 5 May 1997

T. Anderson
Department of Chemical Engineering
University of Florida
Gainesville, Florida

NREL

National Renewable Energy Laboratory

NOTICE

Printed on paper containing at least 50% wastepaper, including 20% postconsumer waste

Table of Contents

SUMMARY

Buffer Layer Processing

High performance CIS or CIGS-based thin film solar cells include the deposition of a thin CdS buffer layer between the CIGS absorber layer and the ZnO window layer. The role of the CdS buffer layer and the impact of the choice of deposition technique, however, are not fully understood. A contactless, nondestructive technique previously developed for the measurement of photogenerated excess carrier lifetimes in SOI wafers was adapted to the study of CIGS. This Dual-Beam Optical Modulation (DBOM) technique has been used to investigate differences between three alternative methods of depositing CdS (conventional chemical bath deposition, MOCVD, and sputtering). The DBOM method monitors the optical modulation of the reflected beam intensity of an IR probe beam ($h\nu < E_g$) incident on the sample. The IR probe beam is modulated by a visible laser pump beam ($h\nu > E_g$) through free carrier absorption in the CIGS film. The fractional change in the transmitted intensity of the IR probe beam is related to the effective lifetime of excess carriers in the absorber material. A simplified model considering reflection at the front CdS surface and the CdS/absorber and absorber/Mo interfaces, and absorption in absorber films was initially developed. During this last period of research, this model was modified to include the presence of a p-n junction at the CdS/absorber film interface. A collaboration with researchers at Purdue University is directed at a more complete simulation of the experiment.

The DBOM tool was used to characterize the free carrier lifetime in CIGS films with and without a CdS buffer layer deposited by various methods. For selected samples, the CIGS surface was treated with a DI water rinse, a Cd-partial electrolyte, or an Ar plasma clean prior to depositing the CdS. A comparison was made of the excess carrier lifetime calculated from the measured modulated probe beam intensity for CdS deposited by sputtering, MOCVD, and CBD. The results reveal that the excess carrier lifetime improves significantly with CdS deposition, regardless of the method used to deposit it. The treatment of the surface with a DI rinse or Cd-partial electrolyte dip showed no

positive influence, nor did a low temperature bake, when compared to the samples not treated prior to CdS growth. In another study, lifetimes were measured in CIGS samples from different sources. Again, the addition of a CdS buffer layer improved the excess carrier lifetime, independent of pretreatment or deposition technique. It is interesting to note that an Ar plasma clean significantly improved the lifetime without the deposition of the CdS buffer layer. XPS analysis of the surface before and after cleaning indicated a shift from an In-rich surface to one close to stoichiometric (Cu/In = 1) upon cleaning. A subsequent change in the extent of band bending or a reduction of the depletion width could have produced the observed increase in DBOM signal. The DBOM technique has proven to be a nondestructive method for rapidly evaluating the quality of CIGS absorber films, although the interpretation of the signal can be complex. Two analytical models were developed to assist in data interpretation.

Thermochemistry and Phase Equilibria in the Cu-In-Se System

A critical assessment of the Cu-In-Se thermochemical and phase diagram data using standard CALPHAD procedures is being performed. The outcome of this research will produce useful information, including equilibrium vapor compositions (required annealing ambients, Se_x fluxes from effusion cells), phase diagrams (conditions for melt assisted growth), chemical potentials (driving forces for diffusion and chemical reactions), and consistent solution models (extents of solid solutions and extending phase diagrams). The assessment work combines thermodynamic data from the literature with models that describe solution behavior in a thermodynamically consistent fashion to estimate solution model parameters and unknown thermodynamic properties.

A reassessment of the Se unary system was initially performed and resulted in revised suggested values for the thermodynamic properties of Se_5 and Se_6. An initial assessment of the In-Se and Cu-Se systems was then done, and conflicting and missing data were identified. To partially fill these gaps, a set of (Cu,In,Se) alloys were synthesized by long time annealing in evacuated ampoules. Quenched samples were characterized for constitution by XRD and DTA, and component activities or Gibbs energies of formation were determined by e.m.f. measurements.

These measurements included a determination of the In activity for the first time in In-rich compositions within and near the two-liquid phase region. Furthermore, the standard Gibbs energies of formation of InSe, In_6Se_7 and In_2Se_3 were derived from e.m.f. data. More recently a series of galvanic cells containing the Cu-In-Se ternary compounds chalcopyrite $CuInSe_2(\alpha)$, sphalerite $CuInSe_2(\delta)$, $Cu_2In_4Se_7$, and $CuIn_5Se_8$ were incorporated into the electrochemical cells to yield the standard Gibbs energy of formation of each compound. A second law value 21.7 kJ/mol was determined for the enthalpy of transformation $CuInSe_2(\alpha)$ to $CuInSe_2(\delta)$, while a third law value of -240 kJ/mol for $\Delta H_{f,298}^o$ of $CuInSe_2(\alpha)$ was calculated from the data. DTA is now being used to determine phase transition temperatures for the alloy compositions synthesized for the electrode materials.

Several collaborations have been initiated to better understand the phase relations in the Cu-In-Se system. In particular, we are working with a group in France (Université de Montpellier), who is performing calorimetric measurements, and in Germany (Max Planck Institut fur Metallforschung), who is doing DTA measurements to compliment our e.m.f. studies. Synthesized ternary samples have been characterized by EXAFS using the new beam line at Argonne National Lab. The same samples are being examined by high resolution NMR in a collaboration with the University of Utah. It is hoped that these investigations will give insight into the local atom arrangements in the defective chalcopyrite compounds and solid solutions. Data previously reported in the literature and recent experimental data were combined to estimate the In_2Se_3-Cu_2Se pseudobinary phase diagram.

Device Processing

An integrated facility to fabricate CIS PV devices has been established that includes Migration Enhanced Epitaxy (MEE) for deposition of CIS, an RTP furnace for absorber film formation, sputtering of ZnO, CBD or MOCVD of CdS, metallization, and pattern definition. One of the key objectives of this program is to identify and test alternative reaction pathways leading to the formation of device quality CIS absorber

layers. Although conventional processes use either stacked elemental layers or a physical amorphous mixture as the precursor material, there may be certain advantages to depositing binary compounds in the precursor film. The phase diagram effort has led to the suggestion of several possible stacked sequences of binary compounds and initial structures have been deposited. Finally, a model was proposed for the role of Na during crystallization of CIS. In this model a Na compound (e.g., $NaInSe_2$ or $Na_3Cu_2In_5Se_{10}$) forms at the surface during recrystallization to control the composition and thus the electrical characteristics of the CIS film. It is hoped the single crystal research will help clarify this model.

LIST OF FIGURES

LIST OF TABLES

INTRODUCTION

This research effort was initiated in May 1995 to develop a novel high-rate processing technique for device quality thin films of CIS-based materials. Important objectives of the program are the development of a plasma-assisted CIS deposition process and subsequent rapid thermal processing of optimized precursor film structures. Fundamental studies on junction formation in CIS, the effects of contaminants such as sodium on the kinetics of the growth and recrystallization processes, and phase equilibria in the Cu-In-Se system are key components of the research program.

A multidisciplinary team is investigating a processing sequence that involves the initial growth of a highly ordered structural template at relatively low rate, followed by the rapid deposition of the bulk of the absorber film's mixed-phase precursor using a plasma-assisted deposition technique. This structure is then rapid thermally processed to recrystallize the film from the seed layer. The high rate deposition system uses either thermally cracked Se or an Electron Cyclotron Resonance (ECR) plasma selenium source. This latter approach promises to reduce the deposition temperature, ensure efficient incorporation of selenium in the film, and provide a driving force at the surface to overcome kinetic limitations of thermal growth at high deposition rate. Through our participation in the Thin Film Partnership Program, we also are exploring an alternative dry process (MOCVD) to deposit buffer layers. We are studying a potentially lower-cost, manufacturable process for conductive, transparent ZnO "window" layer deposition based on DC sputtering from metallic zinc targets using boron or silicon doping. The team is using a variety of characterization techniques, including the development of a new nondestructive and contactless method for measuring electronic defect state lifetimes in CIS films (Dual-Beam Optical Modulation: DBOM).

A second thread of research is directed at obtaining a more fundamental understanding of CIS growth mechanisms. These investigations include study of role of vacancy defect phases at junctions and the effect of "contaminants" such as sodium on

the growth kinetics of CuInSe$_2$. The thermochemistry and phase equilibria in the Cu-In-Se system are being rigorously assessed using the CALPHAD approach and critical missing data are being measured. In particular, solid state galvanic cells are being used to measure component activities in solution and the Gibbs energy of formation of selected compounds. The constitution of the Cu-In-Se system is being predicted from the results of the assessment study and verified at selected overall compositions by DTA and XRD analysis. A result of this activity is the suggestion of alternative routes to the formation of CIS absorber layers.

DBOM STUDY OF BUFFER LAYER PROCESSING

Introduction

Optimization of CuInSe$_2$ (CIS) or Cu(In,Ga)Se$_2$ (CIGS) based thin film solar cells requires the deposition of a thin CdS buffer layer between the CIS/CIGS absorber layer and the ZnO window layer. Considerable effort has been devoted to better understand the role of the CdS buffer layer and the influence of processing procedures on the performance of CIS/CIGS cells. In this program, a contactless, nondestructive reflection mode Dual Beam Optical Modulation (DBOM) technique [1] has been employed to investigate the effects of different CdS deposition techniques (i.e., CBD, MOCVD, and sputtering) on the properties of CIS/CIGS films. The DBOM method utilizes the optical modulation of the reflected beam intensity of an infrared (IR) probe beam ($hv < E_g$) modulated by a visible laser pump beam ($hv > E_g$, e.g., He-Ne laser with $\lambda = 632.8$ nm) via free-carrier absorption in the CIS or CIGS film. The results show that deposition of a CdS buffer layer results in a significant increase in the DBOM signal ($\Delta I/I$). This is related to a change in the free carrier absorption and the excess carrier lifetime in the absorber layer. To explain the observed DBOM results, an analytical model for a CIGS p-n junction cell was derived which contains the functional dependence of $\Delta I/I$ on the surface/interface recombination velocity, excess carrier lifetime, diffusion length, and depletion layer width in the CIS or CIGS cells. The DBOM technique is a nondestructive and contactless method for studying the effects of intermediate processing steps during solar cell fabrication without the confounding effects that subsequent processes might have on the final device characteristics. A detailed comparison of the DBOM data versus different processing steps is also given in this report.

To better understand why a CBD CdS buffer layer works so well in CIGS solar cell structure, the effect of three different deposition processes on the excess carrier lifetimes and material properties of CIGS cells was studied. To be effective, a pinhole-free conformal coverage of the buffer layer is required. Furthermore, the effect of

exchange reactions occurring at the interface of the CdS and CIGS are not well understood. It is possible that Cd or S ions chemically passivate the surface. Also the effect of water rinsing the surface of the CIGS and possible soluble component removable is not clear [2,3]. It is known that Cd binds easily on the surface of a CIGS film [4]. Thus, CdSe or $CdIn_xSe_y$ are suggested to form and be responsible for the graded interface structure [2,3]. In this study, the chemical modification of the CIGS absorber surface by Cd-partial electrolyte treatment, DI water rinsing treatment, and Ar plasma cleaning treatment prior to CdS deposition are also studied. The effects of annealing at 200°C after the intermediate treatments and the MOCVD CdS process on the excess carrier lifetimes in the CIGS films were also reviewed.

Reflection mode DBOM was used to study the effects of various CdS buffer layer processing procedures. Simplified and modified reflection mode DBOM theories are presented. A summary of the DBOM measurement results for CIGS films grown by NREL, SSI and EPV using different growth techniques, deposited by different buffer layer processes, and treated by intermediate surface treatments (i.e., as deposited, DI water rinsed, Cd-partial electrolyte treatment, and Ar plasma cleaned) are also discussed.

Theory

Since CIGS solar cells incorporate a thick Mo backside ohmic contact, DBOM operating in a reflection mode is possible for the measurement of the excess carrier lifetime. The contactless DBOM technique is based on the modulation of the reflected intensity of an infrared (IR) probe beam by a visible pump beam which produces free carrier absorption in the CIGS film. The fractional change in the reflected intensity of the IR probe beam is directly proportional to the excess carrier lifetime in the CIGS film. It is also possible to perform depth profiling of the excess carrier lifetime in the film by changing the wavelength (and hence the absorption depth in the film) of the pump beam. Figure 1 shows a schematic diagram of the reflection mode DBOM experiment designed specifically for lifetime measurements in the CIGS films.
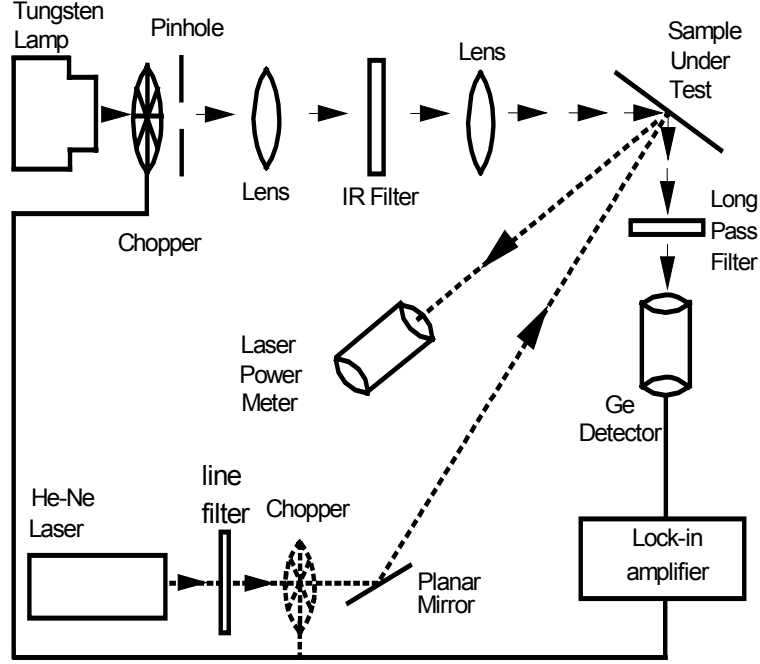
Figure 1. Schematic diagram of reflection mode DBOM setup

A. Simplified Model Without a P-N Junction

To analyze the DBOM data a model is needed to describe the generation transport and recombination of free carriers. The first model developed did not include a p-n junction. The analytical model is described below.

Figure 2 shows the incident and reflected angles of the pump beam and probe beam in the CIGS device structure without a p-n junction. The excess electron density in the CIGS layer can be obtained by solving the continuity equation for electrons and using the boundary conditions at the top ($x = 0$) and bottom interface ($x = t_b$) of the CIGS film, as given by:

$$D_n \frac{\partial^2 \Delta n}{\partial x^2} - \frac{\Delta n}{\tau} + G(x) = 0 \tag{1}$$

$$D_n \frac{\partial \Delta n}{\partial x}\bigg|_{x=0} = s_1 \Delta n(0) \tag{2}$$

$$-D_n \frac{\partial Dn}{\partial x}\bigg|_{x=t_b} = s_2 Dn(t_b) \tag{3}$$

and the generation rate can be expressed as:

$$G(x) = \alpha \phi_0 \cos\theta_3 (1 - R - T)e^{-\alpha x} \tag{4}$$

where α, ϕ_0, R, and T are the absorption coefficient, photon flux, total front surface reflectance, and back-interface transmittance at a given pump beam wavelength, while D_n, t_b, τ, s_1, and s_2 are the diffusion coefficient, CIGS film thickness, excess carrier lifetime, front-surface recombination velocity and back-interface recombination velocity in the CIGS film, respectively.
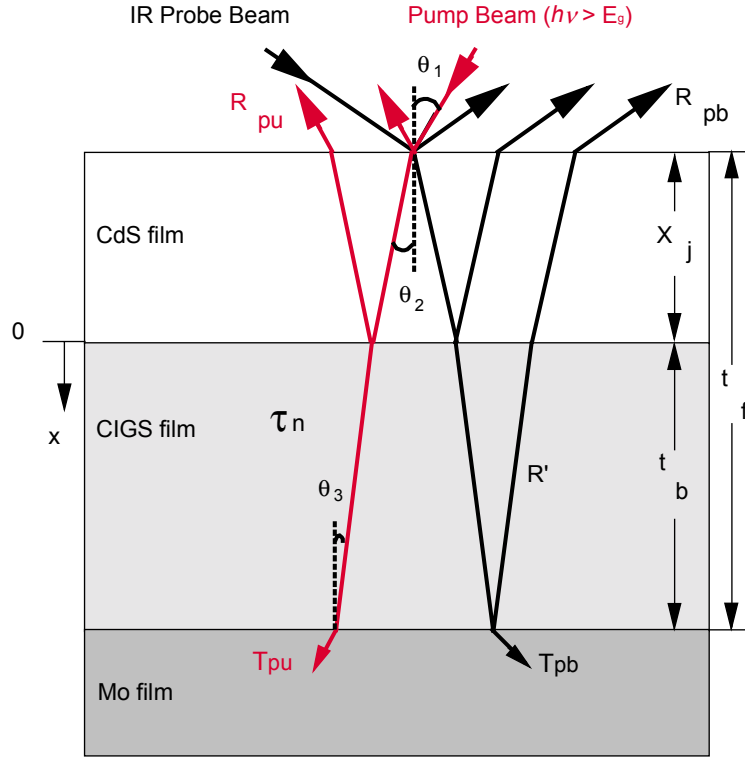
Figure 2. Cross sectional view of CIGS cell used in the simplified DBOM theory

The excess electron density in the CIGS layer as a function of distance along the x-direction can be obtained by solving equation (1), and the result yields:

$$\Delta n(x) = \frac{\alpha \phi_0 (1 - R - T)\cos\theta_3}{D_n \left(\alpha^2 - \frac{1}{L_n^2}\right)} \left(C_1 e^{\frac{x - t_b}{L_n}} + C_2 e^{-\frac{x - t_b}{L_n}} - e^{-\alpha x}\right) \tag{5}$$

where
$$C_1 = \frac{(\alpha D_n + s_1)(\frac{D_n}{L_n} - s_2) - (\alpha D_n - s_2)(\frac{D_n}{L_n} + s_1)e^{-[t_b(\alpha - \frac{1}{L_n})]}}{2[\frac{D_n}{L_n}(s_1 + s_2)\cosh(\frac{t_b}{L_n}) + (s_1 s_2 + \frac{D_n^2}{L_n^2})\sinh(\frac{t_b}{L_n})]} \tag{6}$$

$$C_2 = \frac{(\alpha D_n + s_1)(\frac{D_n}{L_n} + s_2) - (\alpha D_n - s_2)(\frac{D_n}{L_n} - s_1)e^{-[t_b(\alpha + \frac{1}{L_n})]}}{2[\frac{D_n}{L_n}(s_1 + s_2)\cosh(\frac{t_b}{L_n}) + (s_1 s_2 + \frac{D_n^2}{L_n^2})\sinh(\frac{t_b}{L_n})]} \tag{7}$$

In the absence of pump beam excitation, the reflected intensity of the probe beam, I, can be expressed in terms of the unmodulated transmitted intensity I_0, electron density n_0, hole density p_0, and the optical absorption cross-section of electrons and holes, σ_n and σ_p, respectively, as:

$$I = I_0 R' \exp[-2 \int_0^{t_b} (\sigma_n n_0 + \sigma_p p_0) dx] \tag{8}$$

With pump beam excitation the charge neutrality condition yields $\Delta n \cong \Delta p$ $\sim 10^{13} \text{cm}^{-3} << p_0 \approx 10^{16} \sim 10^{18} \text{cm}^{-3}$ for low the injection case. Under low injection conditions, the reflected intensity of the probe beam Iэ can be express as:

$$I' = I_0 R' \exp[-2\Delta N \sigma_{fc} - 2 \int_0^{t_b} (\sigma_n n_0 + \sigma_p p_0) dx] \tag{9}$$

where $\Delta N = \int_0^{t_b} \Delta n(x) dx$

$$= \frac{\alpha \phi_0 (1 - R - T) \cos\theta_3}{D_n(\alpha^2 - \frac{1}{L_n^2})}[L_n C_1(1 - e^{-\frac{t_b}{L_n}}) - L_n C_2(1 - e^{\frac{t_b}{L_n}}) + \frac{1}{\alpha}(e^{-\alpha t_b} - 1)] \tag{10}$$

R' is the reflectance at CIGS/Mo interface, $\sigma_{fc} = \sigma_n + \sigma_p$ is the total optical absorption cross-section of electrons and holes.

For $\Delta I << I$, the fractional change in the probe beam intensity $\Delta I/I$ (with $\Delta I = I' - I$) can be expressed as:

$$\ln(\frac{\Delta I}{I} + 1) \cong \frac{\Delta I}{I} = -2\sigma_{fc}\Delta N$$

$$= -2\sigma_{fc} \left\{ \frac{\alpha\phi_0(1-R-T)\cos\theta_3}{D_n\left(\alpha^2 - \frac{1}{L_n^2}\right)} \left[L_n C_1\left(1-e^{-\frac{t_b}{L_n}}\right) - L_f C_2\left(1-e^{\frac{t_b}{L_n}}\right) + \frac{1}{\alpha}\left(e^{-\alpha t_b}-1\right) \right] \right\} \quad (11)$$

Since the absorption coefficient ($\alpha \approx 8\times10^4$ cm^{-1}) is very high in CIGS at the wavelength of the pump beam (He-Ne laser), and the bulk trap density in CIGS is also high [5,6], the following assumptions prevail for DBOM analysis: (i) $\alpha L_n \gg 1$, (ii) $\alpha D_n \gg s_1, s_2$, (iii) $D_n^2 \gg s_1 s_2 L_n^2$. Based on these assumptions and solving equations (5) through (11), the fractional change in the probe-beam reflected intensity $\Delta I/I$ can be simply expressed as:

$$\frac{\Delta I}{I} = -2\sigma_{fc}\cos\theta_3\phi_0(1-R-T)\tau_{eff}\left(1-e^{-\alpha t_b}\right) \quad (12)$$

where

$$\tau_{eff} = \frac{t_b}{s_1 + t_b/\tau} \quad (13)$$

is the effective excess carrier lifetime in the CIGS film. This term reduces to the bulk film lifetime if the front surface recombination velocity s_1 is much smaller than t_b / τ. Thus, the excess carrier lifetime in a CIGS film can be obtained by using the values of ΔI and I obtained from the DBOM measurements, and the calculated values of R and T.

B. Modified Model with a P-N Junction

Figure 3 illustrates a cw laser impinging upon a CIGS sample with p-n junction. The excess hole concentration $\Delta p(x)$ in the CdS layer and excess electron concentration $\Delta n(x)$ in the CIGS layer can be obtained by solving the continuity equations:

$$D_p \frac{\partial^2 \Delta p(x)}{\partial x^2} - \frac{\Delta p(x)}{\tau_p} + G(x) = 0 \qquad \text{in the CdS layer} \quad (14)$$

and

$$D_n \frac{\partial^2 \Delta n(x)}{\partial x^2} - \frac{\Delta n(x)}{\tau_n} + G(x) = 0 \qquad \text{in the CIGS layer} \quad (15)$$

with boundary conditions given by:

$$D_p \left.\frac{\partial \Delta p(x)}{\partial x}\right|_{x=0} = s_1 \Delta p(0) \qquad [x = 0] \quad (16)$$

$$\Delta p(X_j) = 0 \qquad\qquad [x = X_j] \qquad\qquad (17)$$

$$\Delta n(X_j + W) = 0 \qquad\qquad [x = X_j + W] \qquad\qquad (18)$$

$$-D_n \left.\frac{\partial \Delta n(x)}{\partial x}\right|_{x=t_f} = s_2 \Delta n(t_f) \qquad\qquad [x = t_f] \qquad\qquad (19)$$

and the generation rate G(x) can be expressed as:

$$G(x) = \alpha_{CdS}\phi_0 \cos\theta_3 (1 - R - T)e^{-\alpha_{CdS}x} \qquad \text{in the CdS layer} \quad (20)$$

$$G(x) = \alpha_{CIGS}\phi_0 \cos\theta_3 (1 - R - T)e^{-\alpha_{CIGS}(x+X_j+W)} \quad \text{in the CIGS layer} \quad (21)$$

In these expressions α_{CdS}, α_{CIGS}, ϕ_0, R, and T are the absorption coefficients for CdS and CIGS, photon flux, total front surface reflectance, and back-interface transmittance at a given pump beam wavelength, and D_n, D_p, X_j, W, t_b, τ_p, τ_n, s_1, and s_2 are the diffusion coefficients in the CdS layer and in the p-type CIGS layer, CdS layer thickness, space charge layer thickness, CIGS film thickness, excess carrier lifetimes in the CdS layer and in the p-type CIGS layer, surface recombination velocity in the CdS layer and back-interface recombination velocity in the CIGS film, respectively.
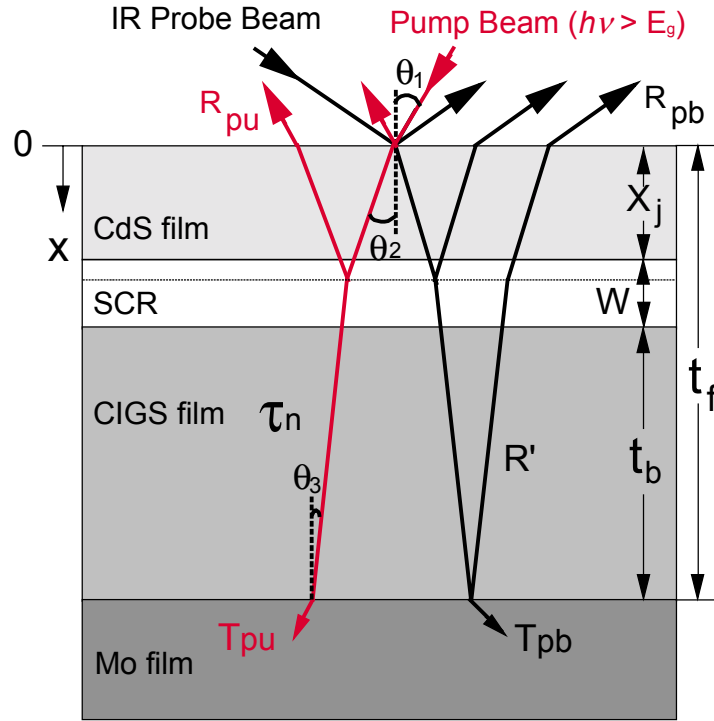
Figure 3. Cross sectional view of CIGS p-n junction cell used in the modified DBOM theory

The excess hole concentration in the CdS layer and excess electron concentration can be obtained by solving equations (14) and (15) with boundary conditions:

$$\Delta p(x) = \frac{\alpha_{CdS}\cos\theta_3\phi_0(1-R-T)}{D_p(\alpha_{CdS}^2 - \frac{1}{L_p^2})} \Bigg| \frac{(\alpha_{CdS}L_p + \frac{L_p}{D_p}s_1)\sinh(\frac{X_j-x}{L_p})}{C_1} + \frac{\frac{L_p}{D_p}s_1\sinh(\frac{x}{L_p})e^{-\alpha_{CdS}X_j}}{C_1}$$

$$+ \frac{\cosh(\frac{x}{L_p})e^{-\alpha_{CdS}X_j}}{C_1} - e^{-\alpha_{CdS}x} \Bigg| \tag{22}$$

$$\Delta n(x) = \frac{\alpha_{CIGS}\cos\theta_3\phi_0(1-R-T)}{D_n(\alpha_{CIGS}^2 - \frac{1}{L_n^2})} e^{-\alpha_{CIGS}(X_j+W)} \Bigg| \cosh(\frac{x-X_j-W}{L_n}) - e^{-\alpha_{CIGS}(x-X_j-W)}$$

$$- C_2\sinh(\frac{x-X_j-W}{L_n}) \Bigg| \tag{23}$$

where $\quad C_1 = \frac{L_p}{D_p}s_1\sinh(\frac{X_j}{L_p}) + \cosh(\frac{X_j}{L_p})$ $\qquad\qquad$ (24)

$$C_2 = \frac{\frac{L_n}{D_n}s_2[\cosh(\frac{t_b}{L_n}) - e^{-\alpha_{CIGS}t_b}] + \sinh(\frac{t_b}{L_n}) + \alpha_{CIGS}L_n e^{-\alpha_{CIGS}t_b}}{\frac{L_n}{D_n}s_2\sinh(\frac{t_b}{L_n}) + \cosh(\frac{t_b}{L_n})} \tag{25}$$

In these equations, θ_3 is the reflection angle of the incident pump beam in the CIGS layer, $t_b = t_f - X_j - W$ is the thickness of the p-type CIS layer, and $L_p = (D_p\tau_p)^{1/2}$ and $L_n = (D_n\tau_n)^{1/2}$ are the diffusion lengths of the minority carriers in the CdS layer and CIS layer, respectively. When the pump beam is turned on, the excess carriers generated in the CIS film will modulate the IR reflected beam intensity. Without the pump beam, the reflected intensity of the probe beam, I, can be expressed in terms of the unmodulated transmitted intensity, I_0, the electron density, n_0, and hole density, p_0, in the absence of pump beam excitation, and the optical absorption cross-section of electrons and holes, σ_n and σ_p, as:

$$I = I_0 R' \exp\left| -2 \int_0^{t_f} (\sigma_n n_0 + \sigma_p p_0) dx \right| \tag{26}$$

Under low injection conditions, the reflected intensity of the probe beam, I', can be expressed as:

$$I' = I_0 R' \exp\left| -2(\Delta N \sigma_{CIGS} + \Delta P \sigma_{CdS}) - 2\int_0^{t_f} (\sigma_n n_0 + \sigma_p p_0) dx \right| \tag{27}$$

where

$$\Delta N = \int_{X_j + W}^{t_f} \Delta n(x) dx \tag{28}$$

$$\Delta P = \int_0^{X_j} \Delta p(x) dx \tag{29}$$

R' is the reflectance at CIGS/Mo interface, $\sigma_{CIGS} = \sigma_n + \sigma_p$ is the total optical absorption cross-section of electrons and holes in the CIGS layer, and σ_{CdS} is the total optical cross-section in the CdS layer.

For $\Delta I << I$, the fractional change in the probe beam intensity $\Delta I / I$ (with $\Delta I = I' - I$) can be solved from equations (26) and (27), and the result yields:

$$\ln\left(\frac{\Delta I}{I} + 1\right) \cong \frac{\Delta I}{I} = -2(\sigma_{CIGS} \Delta N + \sigma_{CdS} \Delta P) \tag{30}$$

$$\frac{\Delta I}{I} = -2\cos\theta_3 \phi_0 (1 - R - T) \left\langle \tau_n \sigma_{CIGS} \frac{\alpha_{CIGS} e^{-\alpha_{CIGS}(X_j + W)}}{\alpha_{CIGS}^2 L_n^2 - 1} \left\{ L_n \sinh\left| \frac{t_f - X_j - W}{L_n} \right| \right. \right.$$

$$\left. - C_2 L_n \left[\cosh\left| \frac{t_f - X_j - W}{L_n} \right| - 1 \right| - \frac{1}{\alpha_{CIGS}} \left[1 - e^{-\alpha_{CIGS}(t_f - X_j - W)} \right] \right]$$

$$+ \tau_p \sigma_{CdS} \frac{\alpha_{CdS}}{\alpha_{CdS}^2 L_p^2 - 1} \left\{ \frac{L_p}{C_1} \left[\cosh\left| \frac{X_j}{L_p} \right| - 1 \left| \left(\alpha_{CdS} L_p + \frac{\tau_p s_1}{L_p} + \frac{\tau_p s_1}{L_p} e^{-\alpha_{CdS} X_j} \right) \right. \right.$$

17

$$+\frac{e^{-\alpha_{CdS}X_j}}{C_1}L_p\sinh\left|\frac{X_j}{L_p}\right|+\frac{1}{\alpha_{CdS}}\left(e^{-\alpha_{CdS}X_j}-1\right)\left|\right\rangle \quad (31)$$

Note that the photon energy of the He-Ne laser ($\lambda_p = 632.8$nm) is smaller than the bandgap energy E_g of CdS and the absorption coefficient α_{CdS} of CdS drops to near zero at the laser wavelength. Furthermore, the thickness of CdS buffer layer used in the CIGS cell is very thin (~500 Å) and the surface recombination velocity, s_1, for CdS layer is large. Thus, the excess carriers, ΔP, generated in the CdS layer are much smaller than those ΔN generated in the CIGS layer. If the excess carriers generated in the CdS layer are negligible, equation (31) becomes:

$$\frac{\Delta I}{I} = -2\cos\theta_3\phi_0(1-R-T)\tau_n\sigma_{CIGS}\frac{\alpha_{CIGS}e^{-\alpha_{CIGS}(X_j+W)}}{\alpha_{CIGS}^2 L_n^2 - 1}\left\{L_n\sinh\left|\frac{t_f - X_j - W}{L_n}\right|\right.$$

$$\left.-C_2 L_n\left[\cosh\left(\frac{t_f - X_j - W}{L_n}\right)-1\right]-\frac{1}{\alpha_{CIGS}}\left[1-e^{-\alpha_{CIGS}(t_f-X_j-W)}\right]\right\} \quad (32)$$

From equation (32) the excess carrier lifetime, τ_n, in the CIGS film can be obtained by using the values of ΔI and I obtained from the DBOM measurements, the calculated values of R and T, and the values of the surface recombination velocity s_2 and the diffusion length L_n of CIGS.

Additional physical insight on the DBOM measurement in CIGS cells was obtained by using the ADEPT (A Device Emulation Program & Tool) device modeling program developed at Purdue University by Prof. J. Gray, who has performed a simulation of the DBOM measurement of CIGS cells [7]. Their modeling focuses on the simulation of minority and majority carrier generation in the CIGS p-n junction, the modulation of the depletion layer and band bending by the majority carriers generated by the pump beam, and the influence of surface and interface states.

Experimental

A. Lifetime Measurement

As illustrated in Figure 1, a tungsten lamp was used as the probe beam which passes through a silicon IR filter with a cutoff wavelength $\lambda_c = 1.5 \ \mu m$. The beam was focused to a size of about 4-mm diameter. A 4 mW He-Ne CW laser ($\lambda = 632.8 nm$) used as the pump beam is focused to a spot size of about 2 mm. Both the probe beam and pump beam was chopped at 405 Hz for synchronous detection by means of a lock-in amplifier. The pump beam was reflected by using half-silver coated mirror that is focused into the same spot as the probe beam on the test sample.

The experimental procedure consisted of first measuring the reflected IR intensity, I, of a DC probe beam with photon energy less than the bandgap energy of the CIGS by chopping the tungsten lamp and detecting the signal with a lock-in amplifier. The change in the reflected beam intensity, ΔI, due to the modulated pump beam with photon energy greater than the bandgap energy of CIGS was measured by using a chopped pump beam superimposed on the probe beam which was not chopped. The resulting IR reflected beam intensity was measured using a lock-in amplifier. From equations (12) and (32), the excess carrier lifetimes in the CIGS films were calculated using the measured values of I and ΔI.

B. Buffer Layer Processing

Three different processing methods (CBD, MOCVD, and sputtering) were used in depositing the CdS buffer layers on the Mo-coated CIGS samples fabricated by National Renewal Energy Laboratory (NREL), Siemens Solar Industries (SSI), and Energy Photovoltaics (EPV) Inc.. Prior to buffer layer processing, intermediate surface treatments (i.e., as deposited, DI water rinsed, Cd-partial electrolyte treatment, and Ar plasma cleaned) were also applied to some of these samples. The DBOM measurements were performed on samples with and without CdS buffer layers deposited by these processing techniques.

CIGS films were grown on soda-lime glass substrates coated with thick Mo films at NREL. The CdS buffer layer was deposited by using the CBD (NREL), sputtering (MRG), and MOCVD (University of Florida) techniques. These samples measured by the DBOM technique were not fabricated into devices but are believed to be comparable to similar samples with cell efficiencies of around 14%. Figure 4 illustrates the processing conditions used in each sample.

Sample number M1517
Sample number M1518

As deposited C	DI water B	Cd electrolyte A

CBD CdS ➤

MOCVD CdS ➤

Sputtering CdS ➤

As deposited C	DI water B	Cd electrolyte A
As deposited F	DI water E	Cd electrolyte D
As deposited I	DI water H	Cd electrolyte G
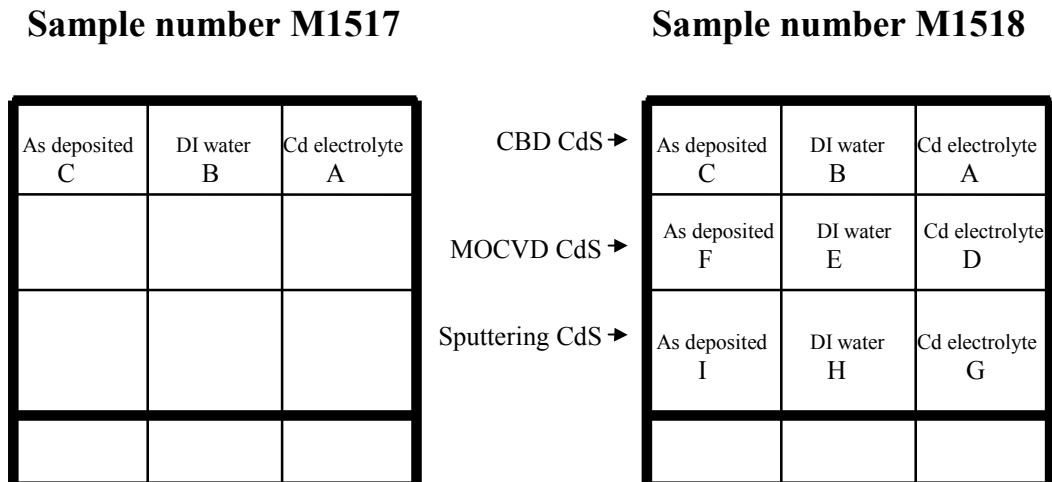
Figure 4. Process conditions for NREL CIGS samples

In addition to the samples fabricated by NREL (Figure 4), CIGS films were provided from two other sources (SSI, EPV). The CdS buffer layers for these samples were deposited by CBD (University of Florida) or sputtering (MRG). The CdS deposition (CBD and sputtering) was carried out on the as-deposited CIGS samples and on the CIGS samples treated with DI water rinsing and Ar plasma cleaning. These samples were characterized by DBOM but not fabricated into solar cells. The films are believed to be comparable to similar samples with efficiencies of about 3 to 5% (highest 9%) that were fabricated by NREL.

Results and Discussion

A. Results Obtained Using the Simplified Model

The following results were obtained using the simplified model (no p-n junction) to analyze the data of ΔI and I measured by the reflection-mode DBOM technique.

The CIGS samples from NREL The results for the NREL CIGS samples were determined by the DBOM technique, and are summarized in Tables 1, 2 and 3, and Figures 5, 6, and 7. Table 1 and Figure 5 show a statistical summary of the excess carrier lifetime taken for the experimental cases of as deposited, after DI water rinsed, after Cd partial electrolyte, and after annealing at $200^{\circ}C$ for 2 minutes for the samples without CdS. Table 2 and Figure 6 summarize the excess carrier lifetime of the samples without CdS and with CBD, MOCVD, and sputtering deposited CdS, and using different surface treatments. For the MOCVD CdS process, Table 3 and Figure 7 show the excess carrier lifetime for each experimental condition: as deposited, after surface treatments, and after MOCVD CdS. It is noted that there is considerable variation in the excess carrier lifetimes for the as deposited CIGS samples without CdS, as are shown in Table 1 and Figure 5, respectively. One of the difficulties in interpreting the DBOM results in these CIGS samples is the fact that we have only CIGS samples with the CBD and sputtered CdS films. Thus, DBOM measurements (and hence the excess carrier lifetime) were not performed on these CIGS samples prior CdS deposition.

Table 1. The excess carrier lifetimes τ_{eff} (ns) of the CIGS samples without CdS

sample #	As	DI water	Cd partial	Annealing
M1517-A	1.46	---	1.34	1.43
M1517-B	1.90	1.73	---	1.75
M1517-C	0.77	---	---	---

Table 2. The average excess carrier lifetimes of NREL samples

	As deposited		DI water rinsed		Cd partial	
	sample #	τ_{eff} (ns)	sample #	τ_{eff} (ns)	sample #	τ_{eff} (ns)
no CdS	M1517C	0.77	M1517B	1.75	M1517A	1.43
CBD CdS	M1518C	3.95	M1518B	2.76	M1518A	3.56
MOCVD CdS	M1518F	17.6	M1518E	1.91	M1518D	4.67
Sputtered	M1518I	12.7	M1518H	7.64	M1518G	5.48

Table 3. The excess carrier lifetimes τ_{eff} (ns) of NREL CIGS samples for MOCVD CdS

sample #	As	DI water rinsed	Cd partial	MOVCD CdS
M1518-D	2.29	---	2.08	4.67
M1518-E	1.71	1.70	---	1.91
M1518-F	0.53	---	---	17.6
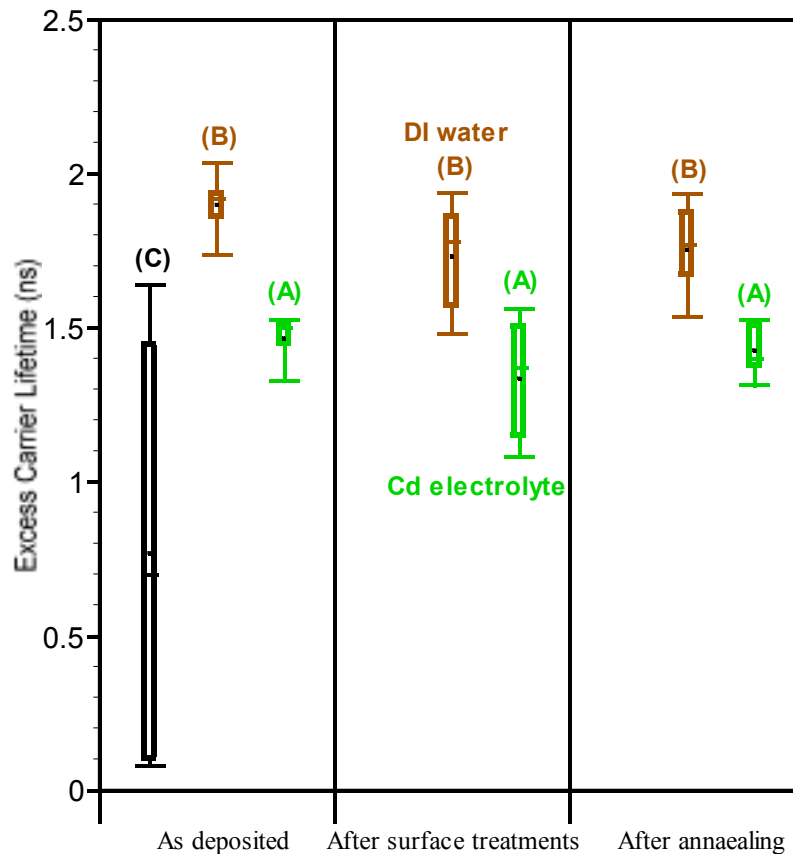
Figure 5. A statistical summary of excess carrier lifetimes for the second set NREL CIGS samples (M1517-A,B, and C), the experimental conditions: as deposited, after surface treatments and after annealing.
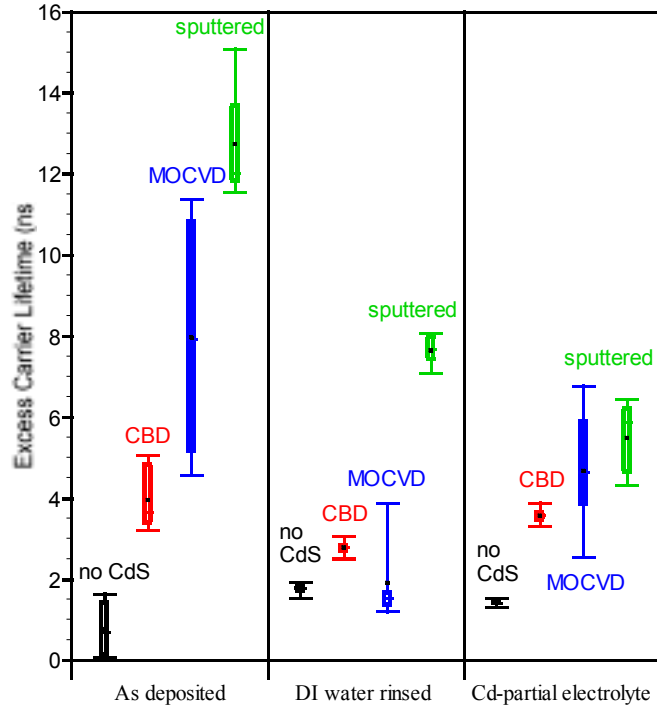
Figure 6. A statistical summary of excess carrier lifetime for the second set NREL CIGS samples without CdS and with CBD, MOCVD, and sputtering deposited CdS and with surface treatments.
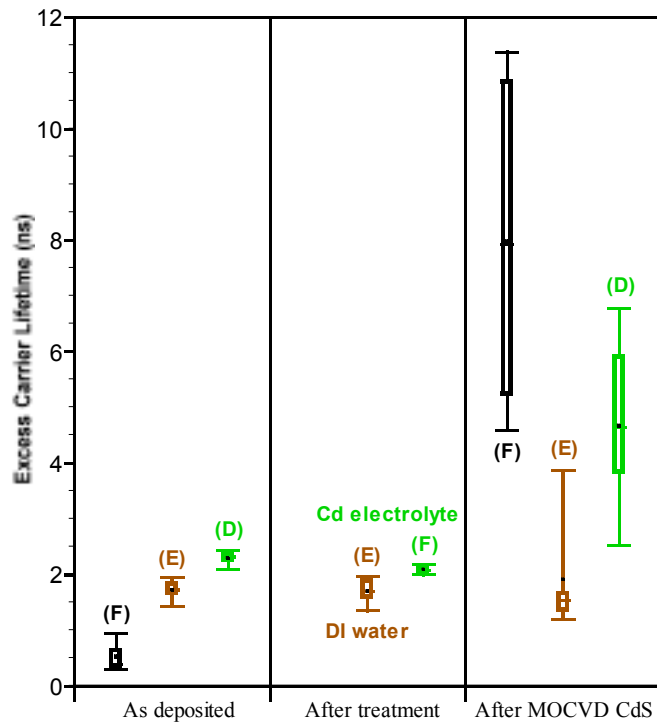
Figure 7. A statistical summary of excess carrier lifetimes for MOCVD CdS deposited CIGS samples

The beneficial effect of CdS deposition on the excess carrier lifetimes in CIGS films is obvious. The results reveal that the excess carrier lifetimes are significantly improved with CdS deposition, with the sputtered CdS deposited CIGS samples showing a dramatic improvement in excess carrier lifetimes for both the as-deposited and after surface treatments. There is no clear evidence, however, of a positive effect of the surface treatments (DI water rinsing and Cd partial electrolyte treatments) and annealing on the excess carrier lifetimes in these CdS deposited CIGS samples or CIGS samples without CdS. It is interesting to note that the most dramatic increase in the excess carrier lifetimes was observed in the sputtered CdS deposited samples with no intermediate surface treatments. Also, the direct processing of sputtered CdS in the as-grown CIGS sample yields the longest excess carrier lifetime when compared to the CdS deposited CIGS samples.

The CIGS samples from SSI and EPV DBOM results for these samples are shown in Figure 8. No detectable DBOM signal was obtained on all CIGS samples unless the CdS buffer layer was present. As with the previous sample set, it is obvious that the CdS buffer layer increases the $\Delta I/I$ values for both the DI water-treated and as-deposited samples. This is especially true for the sputtering CdS deposited CIGS samples which show a dramatic increase in the DBOM signal for those DI water-treated and as-deposited samples (Figure 8). For both the CBD and sputtering CdS deposited samples, the DI water rinsing treatment decreases $\Delta I/I$. It is interesting that the Ar plasma cleaning process significantly increases the DBOM signal for the samples even without the CdS buffer layer. It is possible that Ar ion bombardment on the surface created a smaller depletion width. After Ar plasma cleaning process, XPS data show a clear chemical change near the surface. The Cu/In ratio is restored to around unity although the starting surface composition was heavily In rich. This could be the reason why similar samples fabricated into devices exhibited an increase in V_{oc} or compared to cells fabricated using the as grown and DI water rinsed samples [8]. A smaller depletion width and band bending will have an effect on the results of DBOM measurements, which should give an increase in the DBOM signal. However, after sputter depositing CdS on the CIGS samples the DBOM signal decreases.
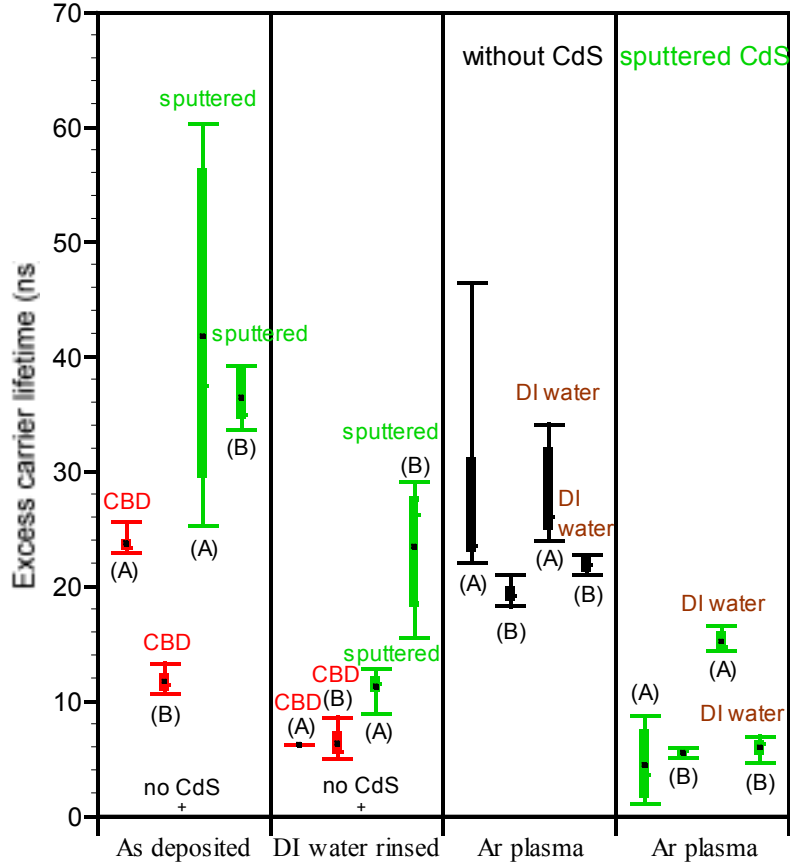
Figure 8. A statistical summary of excess carrier lifetimes for SSI (A) and EPV (B) CIGS samples without CdS and with CBD and sputtering deposited CdS, and with surface treatments

B. Results Obtained By Using The Modified Model

A modified DBOM model was developed to account for the depletion layer effect in the CdS/CIGS p-n junction structure to more accurately interpret the DBOM measurements of the CIGS films. For the NREL CIGS samples with CBD, MOCVD, and sputtering deposited CdS and with surface treatments, Figure 9 shows the average excess carrier lifetime of CIGS films obtained by using the simplified model and the modified model for the following parameter values: surface recombination velocity of the CIGS film, $s_2 = 4 \times 10^6$ cm/sec, depletion width $W = 0.05$ μm, and diffusion length of minority carrier in CIGS film $L_n = 0.6$, 0.68, or 0.7 μm. With equations (25) and (32), the excess carrier lifetime, τ_n, is proportional to the DBOM signal $\Delta I/I$ for the modified model. With

equation (12), the relation between the effective lifetime, τ_{eff}, and the DBOM signal, $\Delta I/I$, for the modified model is similar to the relation for the simplified model. Thus, the lifetimes obtained from simplified and modified models have the same trend, which is clearly shown in the Figure 9 for the specific parameters. The trends identified from application of the simplified model just discussed agree with the results obtained from the modified model.
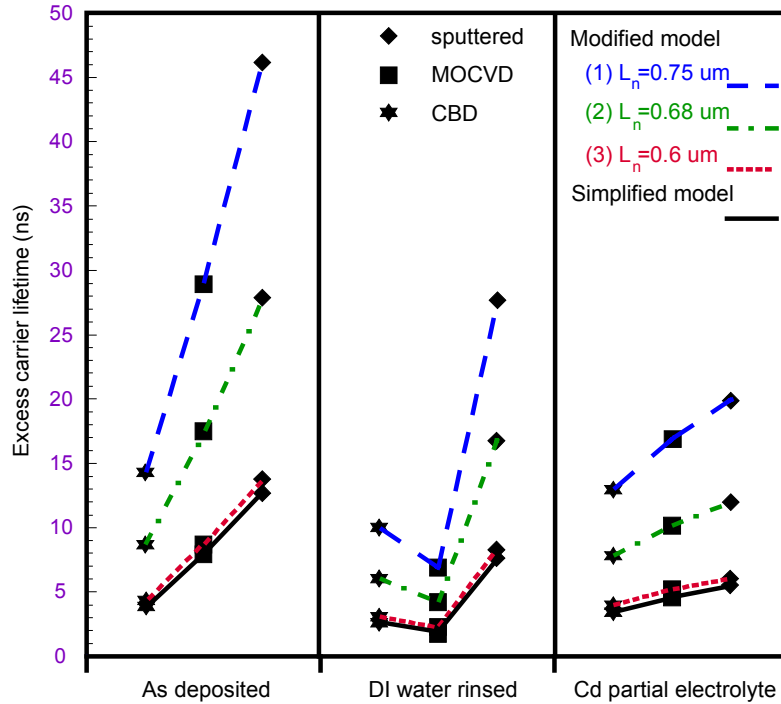
Figure 9. **A comparison of the average excess carrier lifetimes obtained from the simplified and modified DBOM models for the second set NREL CIGS samples with CBD, MOCVD, and sputtering deposited CdS and with surface treatments. (surface recombination velocity $s_2 = 4 \times 10^6$ cm/sec, depletion layer width W= 0.05 μm)**

Figures 10, 11, and 12 show the excess carrier lifetime versus the diffusion length and depletion width for the NREL CIGS samples with CBD, MOCVD, and sputtered deposited CdS, respectively. The excess carrier lifetimes of CIGS films will increase when the diffusion length or depletion width increases. The modified model is more sensitive to the change of the diffusion length than that of the depletion width, while it is

not sensitive to the change of the surface recombination velocity, s_2. Once the diffusion length and depletion width of the CIGS film are determined, the excess carrier lifetime of the CIGS film can be obtained from this modified model.
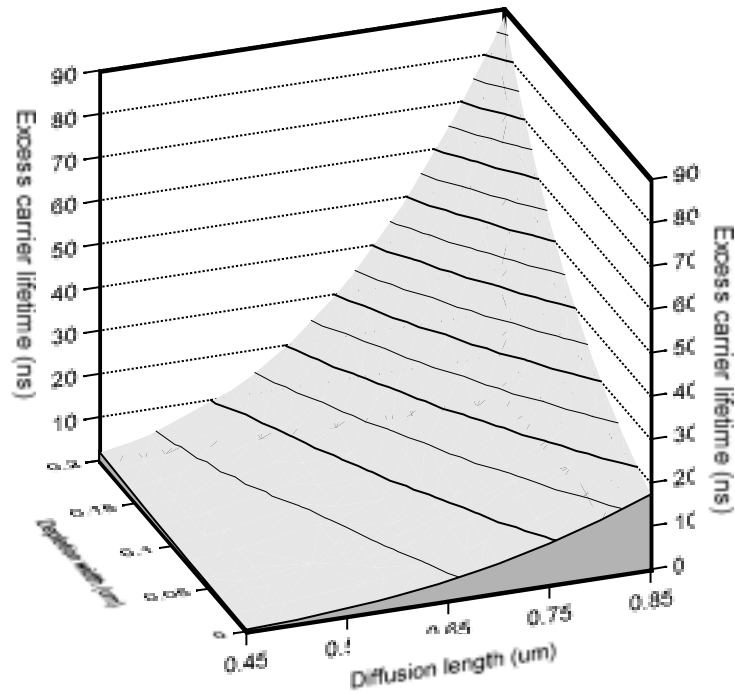
Figure 10. Excess carrier lifetimes of CIGS films versus diffusion length and depletion width for NREL CIGS samples with CBD deposited CdS, determined by modified DBOM theory
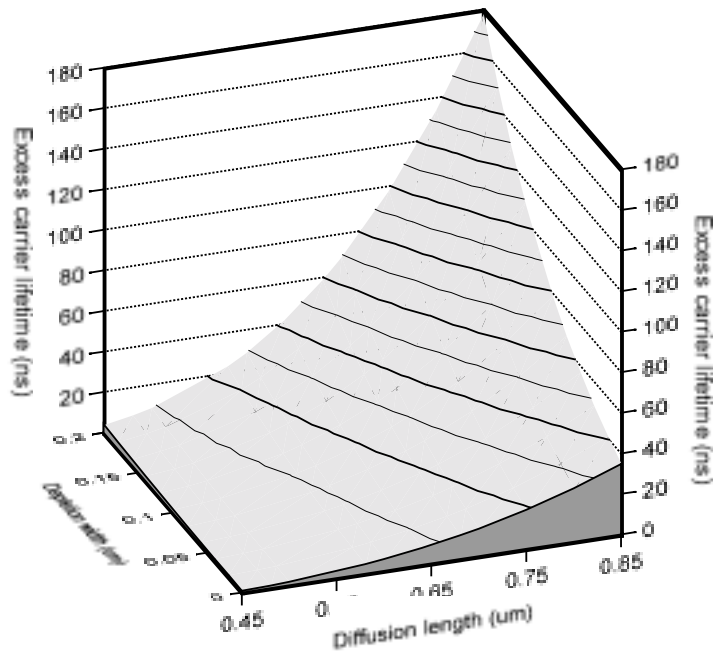
Figure 11. Excess carrier lifetimes of CIGS film versus diffusion length and depletion width for NREL CIGS samples with MOCVD deposited CdS, determined by modified DBOM theory
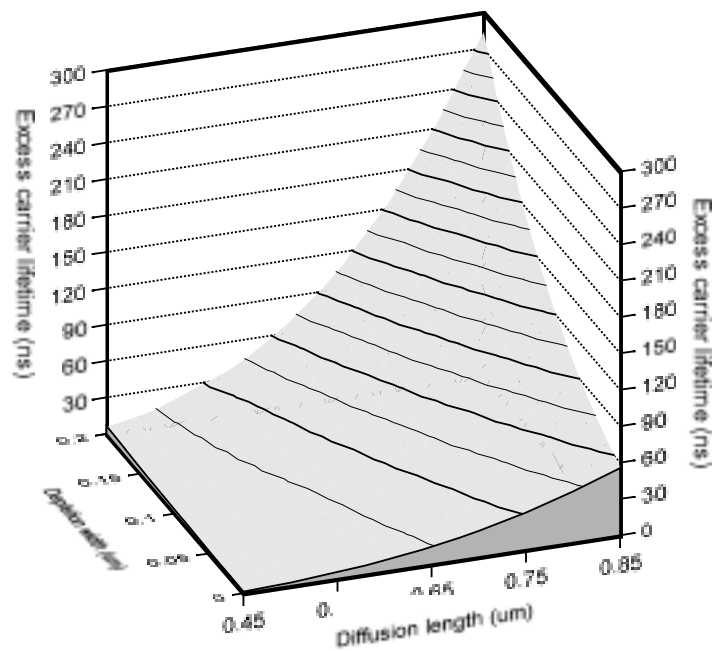
Figure 12. Excess carrier lifetimes of CIGS film versus diffusion length and depletion width for NREL CIGS samples with sputtering deposited CdS, determined by modified DBOM theory

REACTION ENGINEERING AND PRECURSOR FILM DEPOSITION FOR CIS SYNTHESIS

Introduction

A variety of approaches have been used to fabricate thin films in the Cu-In-Se material system as absorbers for photovoltaic devices. Although the absorber films are often referred to as $CuInSe_2$, detailed studies of their crystallographic structure show that the polycrystalline films contain secondary phases [9], including metastable microstructures [10]. Recent comparisons of materials fabricated in different laboratories by different deposition methods [11] and by widely different post-deposition device optimization processes, demonstrate that these inhomogeneities play a significant role in carrier transport processes both within the absorber film, and across its interface with a buffer layer. In recognition of this variability in the actual phase constituents of polycrystalline films used for photovoltaic device fabrication in this material system, they are commonly referred to as CIS films (or CIGS when gallium is incorporated).

Sodium "contamination" of the films due to diffusion from soda lime glass substrates [12] or intentional incorporation during processing [13], has been clearly shown beneficial to device performance when the sodium content is optimized [14]. Reported effects include increased grain size [15], increased acceptor density [16], higher open circuit voltage and fill factor [17], and surface segregation of sodium [18]. The mechanism of sodium's influence on the kinetics of growth and resulting CIS film microstructure and phase constitution is unknown.

A part of this research program is designed to elucidate these issues by combining experimental growth of thin films, synthesis of bulk samples for thermochemical and structural analysis, e.m.f. measurements for determination of Gibbs energies, and a rigorous procedure of critical assessment for evaluation of the thermodynamic consistency of available thermochemical and phase diagram data. The results of these efforts are used to better understand the reaction chemistry of existing techniques for CIS

synthesis and to engineer improved alternatives. This project is specifically directed toward development of a two-stage process for the synthesis of CIS absorber films. The first step is the low temperature deposition of binary precursor films and the second is ex-situ non-equilibrium Rapid Thermal Processing (RTP) to react them and form the desired absorber film structure.

Conventional and Novel Reaction Pathways

The approach of this study differs from that of previously reported RTP approaches, which employ elemental precursor films [19, 20] or attempt direct CIS recrystallization to increase grain size [21]. Conventional processes that synthesize CIS films under reaction conditions closer to equilibrium can be divided into selenization and recrystallization categories. Selenization approaches utilize precursor films predominately of Cu and In, and sometimes containing Ga [22] or minor Te [23] components. The precursor films react with a vapor produced by either the volatilization of condensed selenium or decomposition of hydrogen selenide to form the CIS absorber layer. The reaction chemistry of this approach is extremely complex due to the multiplicity of intermetallic Cu-In phases which can form [24, 25].

The earliest 'recipe' for the synthesis of CIS films for high efficiency photovoltaics (the Boeing bilayer process developed by Mickelsen and Chen [26, 27] is a recrystallization process. In this approach a mixed-phase film layer of $CuInSe_2$ and $Cu_{2-x}Se$ [28] deposited at low temperature reacts with a copper-deficient flux of coevaporated copper, indium, and selenium vapors at higher temperature to optimize the absorber film's stoichiometry during regrowth on the nucleation seeds within the initial layer of the film according to:

$$Cu\ (v) + In\ (v) + Se_n\ (v) \rightarrow CuInSe_2\ (s) + Cu_{2-x}Se\ (s) \quad \text{[precursor deposition]} \qquad (33)$$

$$CuInSe_2\ (s) + Cu_{2-x}Se\ (s) + Cu\ (v) + In\ (v) + Se_n\ (v) \rightarrow CuInSe_2\ (s)\ \text{[regrowth]} \qquad (34)$$
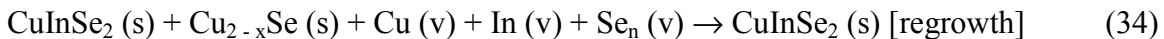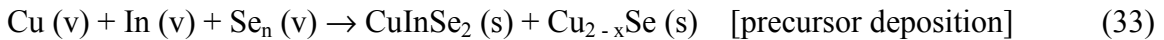
This analysis is based on the assumption of near-equilibrium conditions, and to the extent that non-equilibrium components could be involved under some experimental conditions, a more complex description would be required.

For a final reaction temperature greater than the 523°C monotectic temperature in the Cu-Se binary system [29], significantly increased grain size is observed in the final film [30]. This effect is explained as a consequence of melting of $Cu_{2-x}Se$ in the presence of excess selenium, resulting in a liquid phase assisted regrowth process [31]. Most evidence indicates that the $Cu_{2-x}Se$ phase is in fact not completely consumed during this recrystallization process, with small amounts of $Cu_{2-x}Se$ remaining on the $CuInSe_2$ grain boundaries or as inclusions [32].

This approach has been continuously refined and adapted by many researchers, but apparently different reaction chemistry yielding even higher efficiency devices was developed by Gabor et al. [33]. Their three-stage process for growth is based on the reaction chemistry:

$$In \ (v) + Se_n \ (v) \rightarrow In_2Se_3 \ (s) \qquad \text{[precursor deposition]} \qquad (35)$$

$$In_2Se_3 \ (s) + Cu \ (v) + Se_n \ (v) \rightarrow CuInSe_2 \ (s) + Cu_{1-x}Se_x \qquad \text{[regrowth]} \qquad (36)$$

$$CuInSe_2 \ (s) + Cu_{1-x} \ Se \ (l) + In \ (v) + Se_n \ (v) \rightarrow CuInSe_2 \ (s) \qquad \text{['titration']} \qquad (37)$$
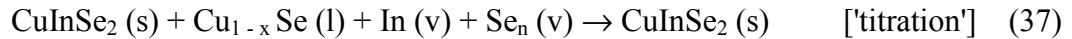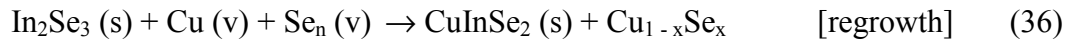
where gallium is typically substituted in part for indium at each step for CIGS synthesis. A two-stage variant of this process omits the final step but carefully controls the total copper flux in the second stage to minimize the Cu_2Se phase in the final film [34]. Both of these reaction sequences are in a sense "inverted" processes with respect to the Boeing bilayer recipe since they begin with an indium sesquiselenide layer and add copper during the second step. The Boeing bilayer process chemistry does not form the indium sesquiselenide at any time.

The approach of this project is designed to realize the manufacturability benefits that RTP offers [35]. From the previous work described above, it appears that essential

components of a successful alternative process are the initial formation of a nucleation seed layer and the subsequent formation of a coexisting liquid phase to achieve large grain size. It further appears that the final growth should occur under indium-rich conditions.

Figure 13 is a composition diagram for the Cu-In-Se ternary system showing the accepted binary selenide compounds and several tie-lines connecting pairs of them, including the pseudobinary tie-line between the binary selenides with the highest melting temperature on each boundary (Cu_2Se and In_2Se_3). In a thermodynamic system closed to mass transfer, the overall reaction product resulting from reacting two compound compositions must lie on that tie-line formed between the reactants, with the location determined by the initial reactant molar ratios.
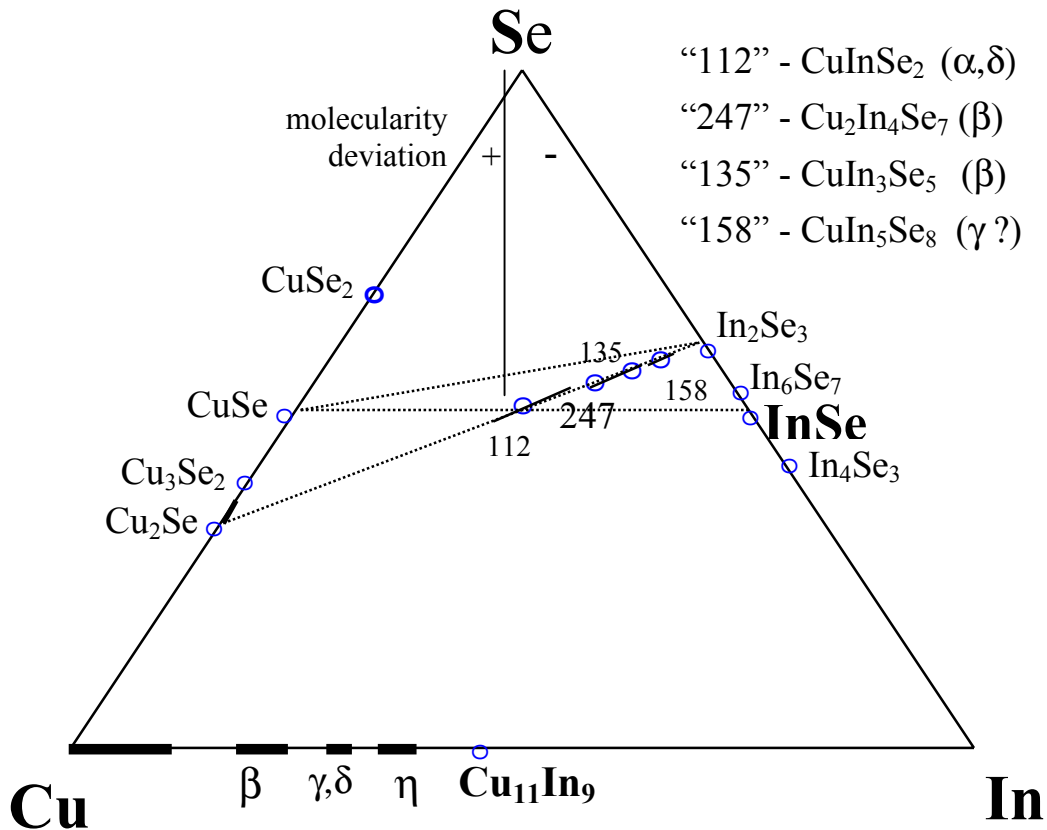
Figure 13. Cu-In-Se ternary composition diagram indicating compounds

Note that two of these tie-lines pass directly through the 112-phase composition (CuInSe$_2$), while the third, connecting the CuSe and In$_2$Se$_3$ phases, does not. This means that a reaction between the latter two binaries cannot yield only the 112 phase in a closed system. Nevertheless this combination is of interest, as will be described below.

First consider the following reaction between Cu$_2$Se and In$_2$Se$_3$ along the pseudobinary tie line to form the 112 phase:

$$Cu_2Se + In_2Se_3 \rightarrow 2CuInSe_2 \tag{38}$$

The ternary composition diagram of Figure 13 can be extended in the third dimension to display temperature, where phase boundaries at various temperatures are represented as embedded two-dimensional manifolds. A cross-section along a tie line through these surfaces yields the phase domains shown in a temperature composition (T-x) diagram. The T-x diagram for the Cu$_2$Se-In$_2$Se$_3$ pseudobinary system was recently assessed [36], as described later in this report, and is reproduced in Figure 14.
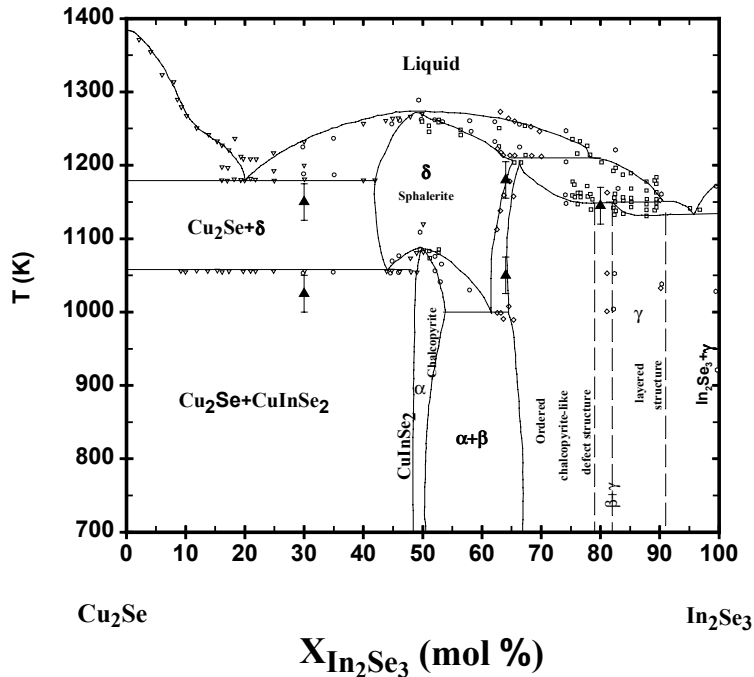
Figure 14. Estimated Cu$_2$Se-In$_2$Se$_3$ pseudobinary phase Diagram

Figure 15 shows the T-x diagrams for the Cu-Se and In-Se systems [36] which comprise two of the three bounding surfaces along the edges of the ternary composition diagram in Figure 13. Inspection of the Cu-Se diagram shows that only liquid phases persist in equilibrium above the 523°C monotectic temperature for overall compositions with more than 52.5 at% selenium. (In,Se) compositions with less selenium than that of the compound In_6Se_7 (<53.8 at% Se) will decompose into a liquid/solid mixture at temperatures above 156 to 600°C (depending on the overall composition), but will not form the high melting temperature compound In_2Se_3 at temperatures below the peritectic decomposition of In_6Se_7 at 660°C. Hence in separate closed systems at equilibrium, appropriately chosen selenium-rich copper binary precursors and selenium-poor indium binary precursors will each exist as liquids or liquid/solid mixtures at temperatures above 523°C to 600°C, and any solid compounds would not be the highest melting-temperature ones found along each of these binary tie-lines, so long as the temperature remains below 660°C.
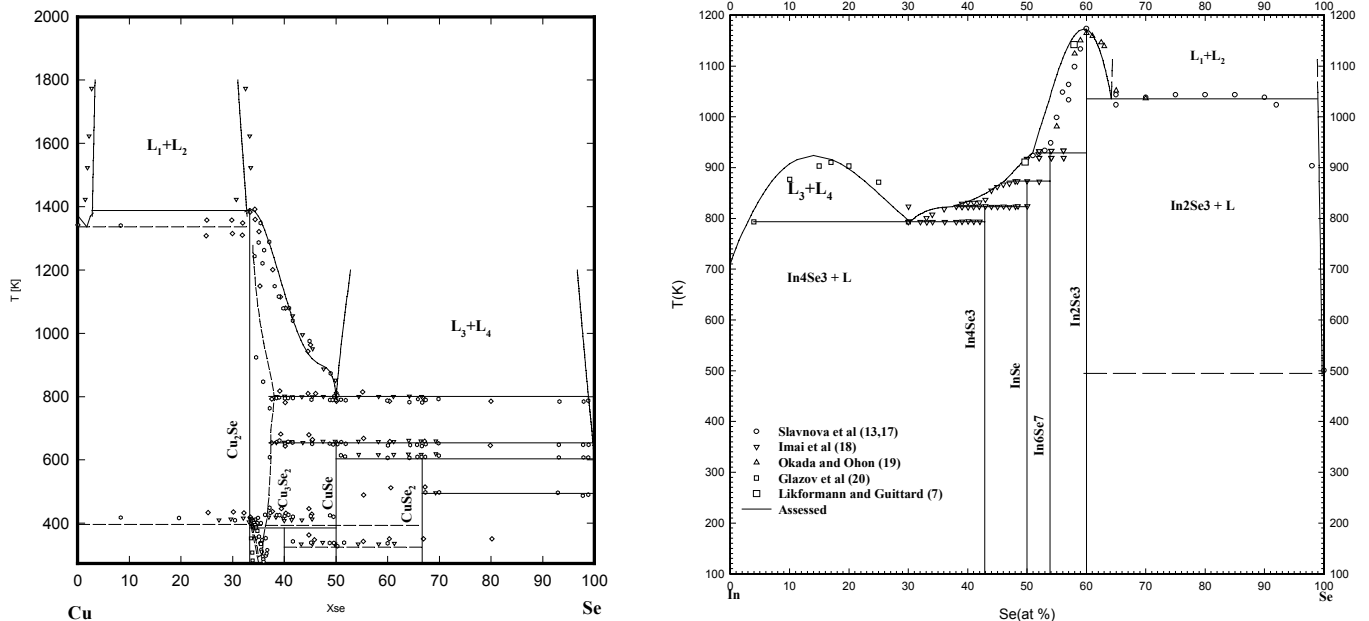
Figure 15. Cu-Se and In-Se binary T-x phase diagrams

These considerations alone do not answer the question of the reactions which would ensue upon liquid-phase mixing of such precursors. The equilibrium result of these reactions is found by reexamination of the T-x sections along the tie lines in Figure 13 between the precursor reactant compositions. Predicted phase diagrams along these other tie-lines suggest the existence of a very low temperature eutectic valley for those which cross the [Cu]/[In] = 1 meridian on the selenium-rich side of the 112 phase, for example the reaction:

$$2CuSe + In_2Se_3 \rightarrow 2CuInSe_2 + Se \tag{39}$$

This eutectic is absent for those tie-lines passing through the stoichiometric 112 composition, reactions such as:

$$CuSe + InSe \rightarrow CuInSe_2 \tag{40}$$

Rapid thermal processing is potentially a nonequilibrium process, which provides an additional degree of freedom for process optimization. If the heating rate of the precursors is faster than the kinetic rate of a given reaction, that reaction may not proceed to its equilibrium extent if the temperature becomes high enough that a competing reaction pathway becomes more favorable. For example, the phase Cu_3Se_2 (see Figure 15) undergoes a peritectoid decomposition into CuSe and $Cu_{2-x}Se$ at a temperature of 112°C. The rate of a solid-solid phase transformation at this low temperature is expected to be very low because substantial atomic rearrangement is required to effect the solid-solid transformation and the atomic transport mechanism is diffusion. Solid state diffusion is many orders of magnitude slower than liquid phase transport processes. Sufficiently rapid heating of Cu_3Se_2 to temperatures in excess of the CuSe peritectic decomposition at 377°C is expected to result in its direct decomposition into $Cu_{2-x}Se$ and selenium-rich liquid phase. Strategies such as this may be useful for circumventing the formation of undesirable reaction byproducts during the RTP synthesis of CIS films from alternative precursors.

Reactant Engineering for Precursor Growth

The underlying motivation for low temperature precursor growth is increased manufacturing equipment throughput, lower equipment cost, and thus a lower amortized capital cost for modules. The deposition of multilayer precursor films for subsequent RTP does not achieve these goals unless isothermal growth conditions can be found. Furthermore, the efficient incorporation of reactants into the precursor film is essential for economical manufacturing.

The fundamental parameters (temperature and flux ratio) for the growth of various phases in the In-Se binary system by means of vacuum coevaporation using elemental reactant fluxes has been thoroughly studied by Emery et al. [37]. Their results show that under polymeric selenium flux-deficient growth conditions there exists a wide temperature domain of monophasic and diphasic stability for the compounds InSe and In$_4$Se$_3$, extending from 225 to at least 400°C. Their analysis [38] suggests that the low sticking coefficient found for selenium is most likely a consequence of the poor thermal accommodation of the larger selenium polymeric species characteristic of Langmuir evaporation from liquid selenium [36].

These authors know no comparably thorough study of the growth of compounds in the Cu-Se binary system. Hence, we have undertaken to determine the parameter domain for the growth of selenium-rich precursor films in a rotating-disc growth system. This growth apparatus incorporates both a conventional double-oven thermal cracking source for selenium and a novel plasma cracker source compatible with both selenium and sulfur. The use of these advanced sources is expected to improve chalcogen sticking coefficients and increase the flux of dimeric and monomeric species. This in turn should reduce growth temperature and source depletion, as observed in the growth of other binary chalcogenides [39].

Wavelength Dispersive Spectroscopy (WDS) analysis of samples from our preliminary experiments at a substrate temperature of ~200°C without cracked or ionized selenium reactants has demonstrated the growth of precursor films with 54 at% selenium which show only the CuSe phase and traces of an unidentified, possibly metastable phase in XRD analysis. Since the CuSe structure is a hexagonal layered one, an excess of selenium could reside either at grain boundaries or intercalated within the grains.

A Model for the Role of Sodium

The phase diagram for the binary Na-Se system shows 5 low temperature selenide compounds. The most stable is Na_2Se, with a melting temperature of 876°C. The phase diagram for the pseudobinary Na_2Se-In_2Se_3 section within the Na-In-Se ternary system has been determined in the composition range of 50 to 100% In_2Se_3 [40]. The existence of two ternary compounds, the 112NIS ($NaInSe_2$) and 135NIS ($NaIn_3Se_5$) was reported but their crystallographic structures were not determined. Eutectics were found at 630°C and 645°C and 7.5 mole% and 42.5 mole% Na_2Se, respectively. These observations may be relevant to the three-layer process or others where In_2Se_3 is grown on sodium-containing substrates or intentionally codeposited with Na_2Se or Na_2S.

These authors know no comparable phase study of the Na-Cu-In-Se quaternary system. Neumann et al. [41] have, however, described a preliminary phase diagram for the system $Cu_{1-x}Li_xInTe_2$. Both of the alkali ternaries $LiInTe_2$ and $NaInSe_2$ differ from either of the copper ternaries $CuInTe_2$ or $CuInSe_2$, in that they do not undergo a chalcopyrite to sphalerite (solid-solid) phase transition at any temperature below their melting temperatures. The pseudobinary phase diagram [41] shows an isothermal chalcopyrite to sphalerite phase transition for alloy compositions between 60 and approximately 80 mole% $LiInTe_2$ and a maximum in the *c* lattice parameter in the same range. This data is evidence for the existence of a tetragonal quaternary compound $Li_3Cu_2In_5Te_{10}$ (corresponding to 60 mole% $LiInTe_2$). It is also possible that the analogous compound $Na_3Cu_2In_5Se_{10}$ may form in the Na-Cu-In-Se quaternary system by the reaction:

$$3NaInSe_2 + 2CuInSe_2 \rightarrow Na_3Cu_2In_5Se_{10} \tag{41}$$
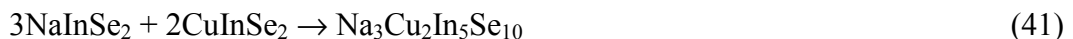
It is conjectured that there exists a wide solid miscibility gap in the Na-Cu-In-Se quaternary system along the $NaInSe_2$-$CuInSe_2$ tie-line in the pseudoternary composition diagram shown in Figure 16, between $CuInSe_2$ and the presumed compound $Na_3Cu_2In_5Se_{10}$. This suggestion that sodium can incorporate into the $CuInSe_2$ lattice to an extent corresponding to the composition range of $CuInSe_2$'s phase stability (a few percent) and segregate to form the compound $Na_3Cu_2In_5Se_{10}$ is both plausible and consistent with numerous observations.

The ratio [In]/([Cu]+[In]) which would be found for a surface-segregated quaternary $Na_3Cu_2In_5Se_{10}$ compound is 5/7 or 71.4%. This is very close to the ratio for the defect chalcopyrite structure $CuIn_3Se_5$, and within the range of values reported for the measured surface ratio [42] for CIS films grown on soda-lime glass.
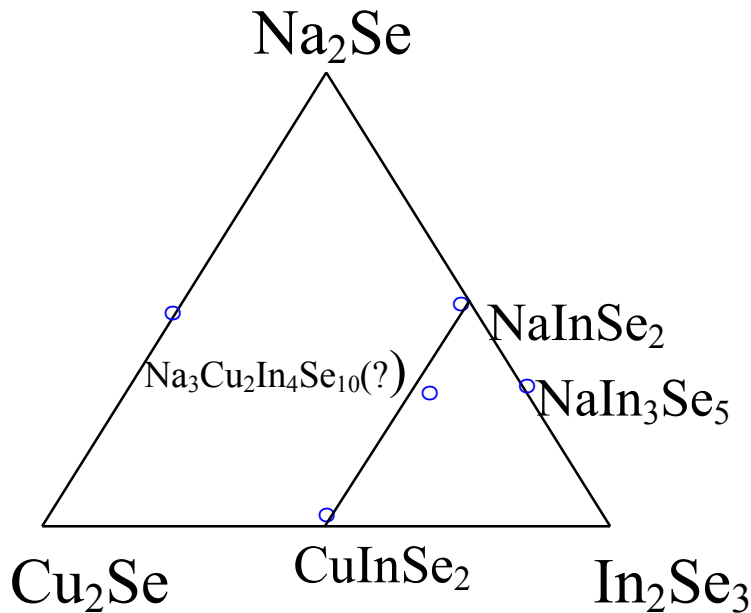
Figure 16. **$NaInSe_2$-$CuInSe_2$ pseudoternary composition diagram**

Electronic transport measurements of CIGS films on Mo-coated soda-lime glass [14] show that sodium incorporation leads to a shallow acceptor state at about 75 meV above the valence band. At high levels of sodium, admittance spectra indicate a high

density of deeper trap states. This suggests a limited range of substitutional incorporation. Our model suggests that this range is determined by the molecularity deviation [43] of the copper chalcopyrite.

XPS and UPS analyses [44] of the chemical shifts and segregation of sodium in CIGS films on Mo-coated soda-lime glass show the presence of two different sodium species, one the consequence of a chemical reaction with environmental H_2O. It is relevant to note that both of the compounds $NaInSe_2$ and $NaIn_3Se_5$ were reported to be unstable in air at room temperature, as is Na_2Se itself.

Summary and Conclusions

A review was presented of some conventional reaction strategies for the synthesis of CIS photovoltaic absorber films from an equilibrium thermochemical perspective, emphasizing the importance of recrystallization and melting processes to their success. Application of these guidelines to non-equilibrium rapid thermal processing of less thermally stable chalcogenide precursor film couples is suggested as a means of further optimizing absorber film synthesis for manufacturability. Our experimental preparation of one such precursor in a novel rotating-disc reactor has been described.

A model was proposed for the chemistry of sodium when present during high-temperature processing of CIS absorbers which is based on the reported existence of the ternary compound $NaInSe_2$ and published phase equilibrium data for the analogous Li-Cu-In-Te quaternary system. We believe that a model based only on a solid solution of Na_2Se and $CuInSe_2$ is insufficient. Available information is inadequate to determine whether a solid solution of $NaInSe_2$ and $CuInSe_2$ ternaries or a quaternary compound such as $Na_3Cu_2In_5Se_{10}$ forms in the Na-Cu-In-Se system as proposed here. It is likely, however, that an accurate model for the influence of sodium on the dynamics of CIS absorber film reaction chemistry will require an answer to this question.

THERMOCHEMISTRY AND PHASE EQUILIBRIA IN THE Cu-In-Se SYSTEM

Introduction

A critical assessment of the Cu-In-Se thermochemical and phase diagram data using standard CALPHAD procedures is being performed. The outcome of this assessment will produce useful information, including equilibrium vapor compositions (required annealing ambients, Se composition from effusion cells), phase diagrams (conditions to form a eutectic melt during annealing), chemical potentials (driving forces for diffusion and chemical reactions), and consistent solution models (extents of solid solutions and consistent point defect structures). The assessment work combines thermodynamic data from the literature with models that describe solution behavior in a thermodynamically consistent manner to estimate solution model parameters and unknown thermodynamic properties.

Our initial assessment revealed a number of inconsistencies in the reported phase diagram as well as a lack of thermodynamic property data for several key compounds, solid solutions, and the liquid phase. This has motivated us to pursue an experimental definition of several specific compounds and solutions, in addition to the modeling work.

Assessment

Our first task was to perform an assessment of the Se unary system since there was an apparent inconsistency between the Gibbs energy of formation of Se_5 and Se_6 and vapor pressure data. The results of this analysis were reported in the Phase I annual report. Our assessment effort was next directed towards the In-Se and Cu-Se binary systems and the assessed phase diagrams of these two systems are presented in the previous section (Figure 15). A preliminary estimation of the pseudobinary Cu_2Se-In_2Se_3 system was next made. The estimated phase diagram is compared to the available experimental data in Figure 14. It is noted that considerable uncertainty exists about the

δ, α, and β solid solution thermodynamics as well as their phase extent. Thus this figure incorporates only estimates for the phase extents.

Experiment

Based on these initial assessments an experimental effort was launched to better define key property values. A set of (Cu,In,Se) alloys was first synthesized by long term anneals in evacuated ampoules to determine the phase constitution by XRD and to provide electrode material to perform e.m.f. measurements for selected compounds in the Cu-In-Se system. An overall summary of the effort is given in Table 4. The preliminary X-ray diffraction analysis of annealed samples shows that the phase boundaries reported in the literature required further justification.   For example, the alloy $(Cu_2Se)_{0.33}(In_2Se_3)_{0.67}$ remained a single phase sphalerite (δ) when quenched from 840ºC, but decomposed to the chalcopyrite (α) and defect-chalcopyrite (β) phases after re-annealing at 650ºC. This implies that the δ phase has a wider homogeneity range than previously reported.   The measured lattice parameters for the chalcopyrite-like and sphalerite structures are listed in Table 5 along with the estimated compositions for these phases.

Table 4. Summary of experimental and assessment accomplishments

	Experiments Conducted			Assessment
System*	**XRD**	**DTA**	**e.m.f.**	**(CALPHAD)**
Se				
In-Se				
Cu-Se				
Cu-In-Se				**preliminary**

* The pure Cu, In and binary Cu-In systems are considered well established.

Table 5. Crystal parameters and estimated compositions for selected ternary phases in the Cu-In-Se system

Phase	Approximate Composition used for XRD $(Cu_2Se)_{1-x})(In_2Se_3)_x$	Lattice Type	Lattice Parameters
α	x=0.50	chalcopyrite	a = 5.780 ± 0.003 c = 11.577 ± 0.008
δ	x=0.67	sphalerite	a = 5.752 ± 0.005
β	x~0.68	defect-chalcopyrite	a = 5.747 ± 0.005 c = 11.62 ± 0.03
γ	to be determined		

The Gibbs energies of formation of the synthesized compounds were determined in solid state electrochemical cells. A review of the literature showed that although several studies of the Cu_2Se-In_2Se_3 pseudobinary system [36, 45-53] have been reported, the thermodynamic properties of several compounds are not well understood. In our work we investigated four ternary compounds $CuInSe_2$ (both α and δ phases), $Cu_2In_4Se_7$, $CuIn_3Se_5$ and $CuIn_5Se_8$.

As previously mentioned there is considerable ambiguity in the literature [54-58] on the phase transformation of chalcopyrite (α phase) to sphalerite (δ phase) $CuInSe_2$. Thermodynamic data on the stability of the other ternary phases, however, are scarce. The most extensively studied phase is the α phase of $CuInSe_2$. Berger et al. [59] reported a value for the standard enthalpy of formation, $\Delta H°_{f,298}$, of α $CuInSe_2$ based on their mass spectrometry data. A value for $\Delta H°_{f,298}$ for the α phase has also been estimated by Glazov et al. [60] using the dielectric bonding theory of Phillips and Van Vechten [61] and spectroscopic and structural data. Gombia et al. [62] calculated a value from the heats of atomization reported by Neumann [63]. Bachmann et al. [64] measured the low temperature heat capacity of the α phase by pulsed calorimetry and derived the absolute entropy, $S°_{298}$, while Neumann [65] measured the high temperature heat capacity in the temperature range 300 to 500 K. Lamoreaux et al. [66] determined the enthalpy of

formation of $CuInSe_2$ using data from mass spectroscopic studies. Cahen and Mirovsky [67] calculated values of $\Delta G°_f$ for the α phase based on the work by Lamoreaux et al. [66] and Bachmann [64].

Very little data exists for the other solid phases. Khriplovich et al. [68] measured the low temperature heat capacity of $CuIn_2Se_{3.5}$ in the temperature range 5 to 300 K. More recently, Wei et al. [54,69] calculated the enthalpy of formation of several ternary compounds by first principle calculation.

We have determined the relative stabilities of these four ternary compounds by measuring open circuit potentials in solid state electrochemical cells with electrodes containing the α phase and co-existing ternary phases.

The e.m.f. measurements were made on the following galvanic cells:

W | In (l), In_2O_3 (s) || YSZ || In_2O_3 (s), Cu (s), Cu_2Se (s), $CuInSe_2$ (α or δ) | C | W   (I)

W | In (l), In_2O_3 (s) || YSZ || In_2O_3 (s), $Cu_2In_4Se_7$ (s), $CuInSe_2$ (α or δ), InSe (s or l)

  | C | W   (II)

W | In (l), In_2O_3 (s) || 15YSZ || In_2O_3 (s), $CuIn_5Se_8$ (s), $CuIn_3Se_5$ (s), InSe (l)

  | C | W   (III)
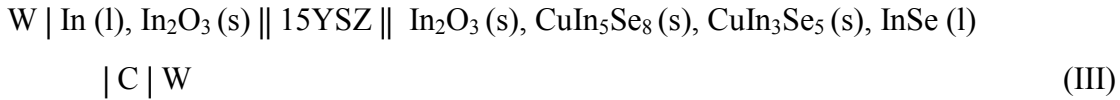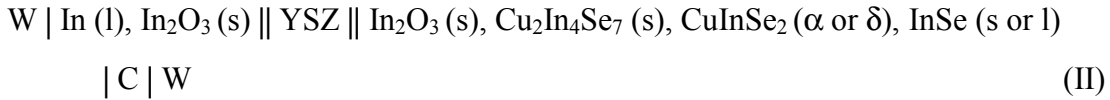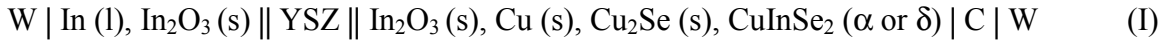
The working electrodes of the electrochemical cells were formed by intimate mixing of the co-existing phases, including the addition of In_2O_3 to about 30% by mass. The reference electrode was made identical in each cell studied and was (0.88 In + 0.12 In_2O_3). High density, nuclear grade graphite cups were used to contain the test electrode material. The absence of asymmetric potentials produced by the graphite cup was tested by measuring the symmetrical galvanic cell with identical (In/In_2O_3) electrodes. Within experimental error, the measured e.m.f. was zero for the above symmetric cell over the temperature range 900 to 1200 K. A small flow of purified argon at slightly above atmospheric pressure was provided for the electrodes of the cell compartment. The

temperature of the cell was measured using a Pt-10%Rh/ Pt thermocouple whose junction was located near the electrodes of the cell in the isothermal zone of the furnace. The reversibility of the e.m.f. readings was ascertained by their reproducibility in thermal cycling as well as by micropolarization. The achievement of equilibrium was further verified by incorporating 5 to 10% variation in the composition of the co-existing phases of the test electrodes from one experimental run to the other. The working electrodes were examined by XRD at the end of each experiment to confirm the phase composition remained the same. A more complete experimental description is given elsewhere (70, 71).

Results and Discussion

The measured open circuit potentials of cells I, II and III are given in Figures 17, 18 and 19. As can be seen in these figures, the open circuit potentials exhibit two distinct lines in cell I and three lines in cell II. A regression analysis of each linear segment produced the following parameter values:

$$(E_{I(a)} \pm 1.55) \quad (mV) \quad = \quad -330.82 + 0.41386\ T(K)\ (949\ to\ 1044\ K) \quad\quad (42)$$

$$(E_{I(b)} \pm 0.41) \quad (mV) \quad = \quad -405.74 + 0.48696\ T(K)\ (1055\ to\ 1150\ K) \quad\quad (43)$$

$$(E_{II(a)} \pm 0.65) \quad (mV) \quad = \quad -311.49 + 0.38268\ T(K)\ (868\ to\ 923\ K) \quad\quad (44)$$

$$(E_{II(b)} \pm 1.02) \quad (mV) \quad = \quad -227.07 + 0.29204\ T(K)\ (935\ to\ 1045\ K) \quad\quad (45)$$

$$(E_{II(c)} \pm 1.70) \quad (mV) \quad = \quad -377.20 + 0.43496\ T(K)\ (1054\ to\ 1179\ K) \quad\quad (46)$$

$$(E_{III} \pm 2.53 \quad (mV) \quad = \quad -519.57 + 0.54917\ T(K)\ (977\ to\ 1145\ K) \quad\quad (47)$$

A. α to δ Transition in CuInSe$_2$
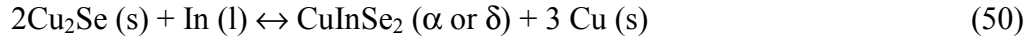
The half-cell reactions of cell I can be written as:

$$1/2\ In_2O_3\ (s) + 2Cu_2Se\ (s) + 3e^- \leftrightarrow CuInSe_2\ (\alpha\ or\ \delta) + 3Cu\ (s) + 3/2\ O^{2-} \quad (48)$$

and

$$In\ (l) + 3/2\ O^{2-} \leftrightarrow 1/2\ In_2O_3\ (s) + 3e^- \tag{49}$$

For the passage of 3 Faraday equivalents, the overall cell reaction can be represented as:

$$2Cu_2Se\ (s) + In\ (l) \leftrightarrow CuInSe_2\ (\alpha\ or\ \delta) + 3\ Cu\ (s) \tag{50}$$

Thus the measured potential of cell I is related to the standard Gibbs energy change:

$$\Delta G^\circ_{R(\alpha\ or\ \delta)} = \Delta G^\circ_f\ CuInSe_2\ (\alpha\ or\ \delta) - 2\ \Delta G^\circ_f\ Cu_2Se\ (s) \tag{51}$$

Using the Nernst equation results in the following expressions:

$$(\Delta G^\circ_{R(\alpha)} \pm 0.45)\ (kJ/mol) = 95.76 - 0.11980\ T(K) \tag{52}$$

$$(\Delta G^\circ_{R(\delta)} \pm 0.12)\ (kJ/mol) = 117.45 - 0.14096\ T(K) \tag{53}$$

Since there is no phase transition in Cu_2Se, In, and Cu in the temperature range 949 to 1150 K, the difference in ΔG°_R calculated from equations (52) and (53) correspond to the standard Gibbs energy change $\Delta G^\circ_{R\ (\alpha\ -\ \delta)}$ for the α to δ transition in $CuInSe_2$. When the Gibbs energy difference is zero, the values of 1025 K and 21.7 kJ/mol are calculated for the transition temperature and the standard enthalpy of transition,
$\Delta H^\circ_{\alpha \to \delta}$ for $CuInSe_2$.

For cell II, the overall cell reaction can be represented as:

$$Cu_2In_4Se_7\ (s) + In\ (l) \leftrightarrow 2CuInSe_2\ (\alpha\ or\ \delta) + 3InSe\ (s\ or\ l) \tag{54}$$
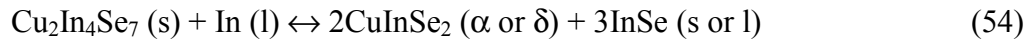
As in the case of cell I, using the e.m.f. expressions (45) and (46) yields values of 1050 K and 21.7 kJ/mol for the $\alpha \to \delta$ transition temperature and $\Delta H^\circ_{\alpha\ -\ \delta}$ for $CuInSe_2$. Considering these are derivative data, the agreement with the results from cell I is very good. The two calculated transition temperatures, 1025 and 1050 K obtained from cells I and II, are in good agreement with the value 1083 K reported by Palatnik and Rogacheva

[45], Mechkovski et al. [56] and Shay and Wernick [72]. The value of the enthalpy change, however, is considerably larger than the value estimated by Wei et al. [54] using Monte Carlo simulation (transition temperature = 1125 ($\pm$20) K and $\Delta H^{\circ}_{\alpha \to \beta}$ =5.0 kJ/mol) and the DTA result of Garbato et al. [58] ($\Delta H_{\alpha \to \delta}$ = 8.0 kJ/mol). These values are compared in Table 6.

B. Phase Transition in InSe (s or l)

The e.m.f. equations (44) and (45) are valid for the solid and liquid ranges of existence of InSe, respectively. Combining these two results, the standard Gibbs energy change for the melting transformation of InSe , ΔG°_{fus}, was derived as:

$$(\Delta G^{\circ}_{fus} \text{ (InSe)} \pm 0.49) \text{ (kJ/mol)} = 8.15 + 0.00875 \text{ T (K)} \tag{55}$$

The melting temperature and the standard enthalpy of fusion of InSe were calculated to be 931 K and -8.2 kJ/mol, which are in very good agreement with the value 933 K reported by Mills [73] and the value -9.6 kJ/mol reported by Vassilev et al. [74].

C. Standard Gibbs Energy of Formation of CuInSe$_2$

The values of the Gibbs energy of formation of the α and δ phases were calculated using the expressions in (52) and (53) along with the following expression for ΔG°_f of Cu$_2$Se determined experimentally using a similar technique:

$$(\Delta G^{\circ}_f \text{ Cu}_2\text{Se} \pm 0.68) \text{ (kJ/mol)} = -86.36 - 0.01534 \text{ T (K) (853 to 983 K)} \tag{56}$$

The standard Gibbs energies of formation of CuInSe$_2$ in the (α) or (δ) phase were then calculated and are given as:

$$(\Delta G^{\circ}_f \text{ (CuInSe}_2, \alpha) \pm 1.13) \text{ (kJ/mol)} = -76.96 - 0.08912 \text{ T (K)} \tag{57}$$

$$(\Delta G^{\circ}_f \text{ (CuInSe}_2, \delta) \pm 0.80) \text{ (kJ/mol)} = -55.27 - 0.11028 \text{ T (K)} \tag{58}$$

Table 6. Comparison of T_{trans} and ΔH^o_{trans} of CuInSe$_2$

Solid Phase	T_{trans} (K)	ΔH^o_{trans} (kJ/mol)	Reference
CuInSe$_2$	1058-1083	-	[55]
	1083	-	[45,56,72]
	1125	5.0	[54]
	-	8.0	[58]
	1025	21.7	This work (from Cell I)
	1050	21.7	This work (from Cell II)

Table 7. Computation of ΔG^o_f of Ternary Compounds in Cu-In-Se System

Compounds	ΔG^o_f (kJ /mol) A+ BT (K)		T Range (K)	ΔG^o_f (kJ /mol) at 1000 K
	A	B		
CuInSe$_2$ (α)	-76.96	-0.08912	949-1044	-166.08
CuInSe$_2$ (δ)	-55.27	-0.11028	1055-1150	-165.55[*]
Cu$_2$In$_4$Se$_7$ (s)	-681.48	-0.11562	868-1179	-565.86
CuIn$_3$Se$_5$[**] (s)	-472.90	-0.0622	-	-535.10
CuIn$_5$Se$_8$ (s)	-1086.56	+0.31049	977-1145	-776.07

* extrapolated value   ** estimated using literature values

D. Standard Gibbs Energy of Formation of $Cu_2In_4Se_7$ (s)

The e.m.f. expression (44) corresponds to the overall galvanic cell reaction given in equation (54) and corresponds to a Gibbs energy change:

$$(\Delta G°_{R(54)} \pm 0.19) \text{ (kJ/mol)} = 90.16 - 0.11077 \text{ T (K)} \tag{59}$$

The above equation was combined with equation (57) and with the following preliminary expression for $\Delta G°_f$ of InSe determined in the work:

$$(\Delta G°_f \text{ (InSe, s)} \pm 1.24) \text{ (kJ/mol)} = -144.82 + 0.06045 \text{ T (K)} \tag{60}$$

to yield the $\Delta G°_f$ of $Cu_2In_4Se_7$.

$$(\Delta G°_f \, Cu_2In_4Se_7 \text{ (s)} \pm 2.56) \text{ (kJ/mol)} = -678.54 - 0.11388 \text{ T (K)} \tag{61}$$

By combining the expression for $\Delta G°_f$ (InSe, l) along with the standard Gibbs energy change expressions obtained from equations (45) and (46) and the appropriate $\Delta G°_f \, CuInSe_2$ expressions, two additional expressions for $\Delta G°_f \, Cu_2In_4Se_7$ (s) are obtained over the extended temperature range of 935 to 1045 K and 1054 to 1179 K, respectively. The following expression is then suggested for the standard Gibbs energy of formation of $Cu_2In_4Se_7$ in the temperature range 868 to 1179 K:

$$(\Delta G°_f \, Cu_2In_4Se_7 \text{ (s)} \pm 2.56) \text{ (kJ/mol)} = -681.48 - 0.11562 \text{ T (K)} \tag{62}$$

E. Stability of $CuIn_5Se_8$

The e.m.f. expression given by equation (47) corresponds to the overall cell reaction (cell III):

$$CuIn_5Se_8 \text{ (s)} + In \text{ (l)} \leftrightarrow CuIn_3Se_5 \text{ (s)} + 3 \, InSe \text{ (l)} \tag{63}$$
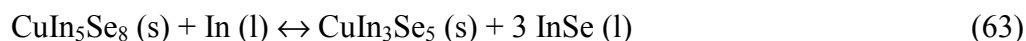
with a calculated Gibbs energy change

$$(\Delta G°_{R \, (63)} \pm 0.73) \text{ (kJ/mol)} = 150.40 - 0.15896 \text{ T (K)} \tag{64}$$

The following data for ΔG°_f of $CuIn_3Se_5$ (another β phase) was estimated. Using the calculated values of $\Delta H^{\circ}_{f,298}$ of Wei [69], an estimate for S°_{298}, and neglecting the ΔC_P terms, the following Gibbs energy expression is produced:

$$(\Delta G^{\circ}_f\, CuIn_3Se_5\, (s))\, (kJ/mol) = -472.90 - 0.06220\, T\, (K) \qquad (65)$$

By combining equations (64) and (65) with ΔG°_f (InSe, l) values from the literature, the standard Gibbs energy of formation of $CuIn_5Se_8$ is given as:

$$(\Delta G^{\circ}_f\, of\, CuIn_5Se_8 \pm 1.97)\, (kJ/mol) = -1086.56 + 0.31051\, T\, (K) \qquad (66)$$

F. Computation of $\Delta H^{\circ}_{f,298}$ of $CuInSe_2$ (α) and $Cu_2In_4Se_7$ (s)

To assess potential temperature dependent errors in the e.m.f. measurements of cell I and their consistency with the calorimetric data, a third-law analysis was performed. For this purpose, the values of the free energy functions for Cu, In, Se and $CuInSe_2$ from Cahen and Noufi [75] were combined with the ΔG°_R values calculated from each e.m.f. value along with ΔG°_f of Cu_2Se at each experimental temperature. A third-law plot of $\Delta H^{\circ}_{f,\,298}$ $CuInSe_2$ is shown in Figure 20. The mean value of $\Delta H^{\circ}_{f,\,298}$ $CuInSe_2$ was found to be -200.96 ± 6.6 kJ/mol. The slight temperature dependence in the ΔH°_{298} values could be the result of temperature dependent errors either in the present e.m.f. data, the free energy functions, or the standard Gibbs energy of formation of Cu_2Se. The free energy functions for each $CuInSe_2$ phase was derived from the low temperature (300 to 500 K) heat capacity data of Neumann [63] and extrapolated to high temperature. A comparison of the literature values for ΔH°_{298} along with the value for S°_{298} is given in Table 7.

Because of the paucity of data for the free energy functions for the β phase, $Cu_2In_4Se_7$, no third-law analysis was performed for this composition. Assuming the value of $\Delta H^{\circ}_{f,\,997}-\Delta H^{\circ}_{f,\,298}$ for the β phase is comparable to $CuInSe_2$, the $\Delta H^{\circ}_{f,\,298}$ for $Cu_2In_4Se_7$ was estimated to be -805.5 kJ/mol.
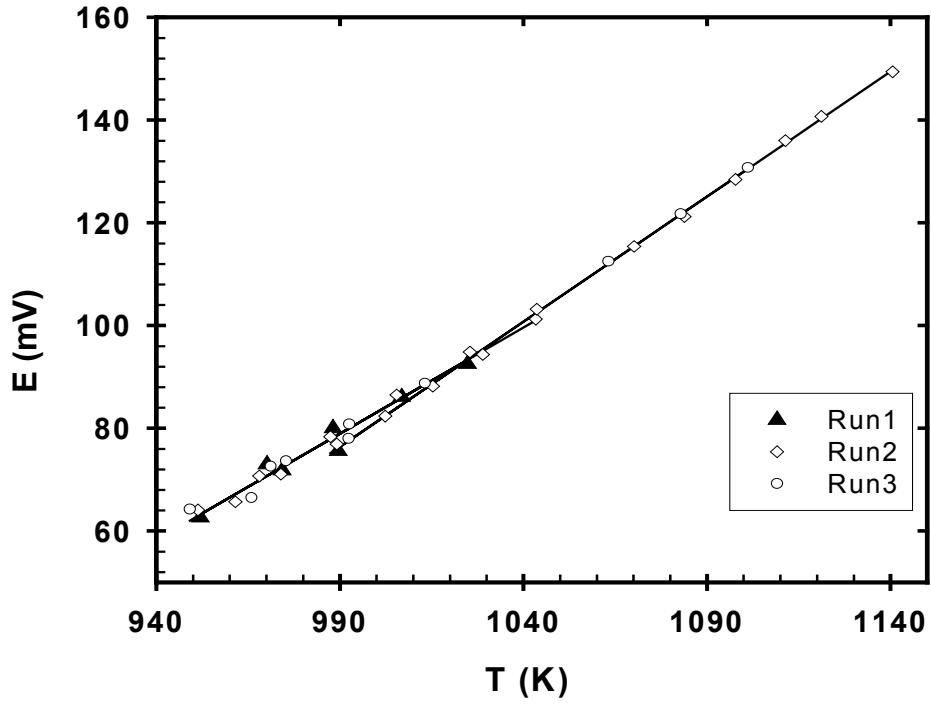
Figure 17. Temperature dependence of the e.m.f. of cell I
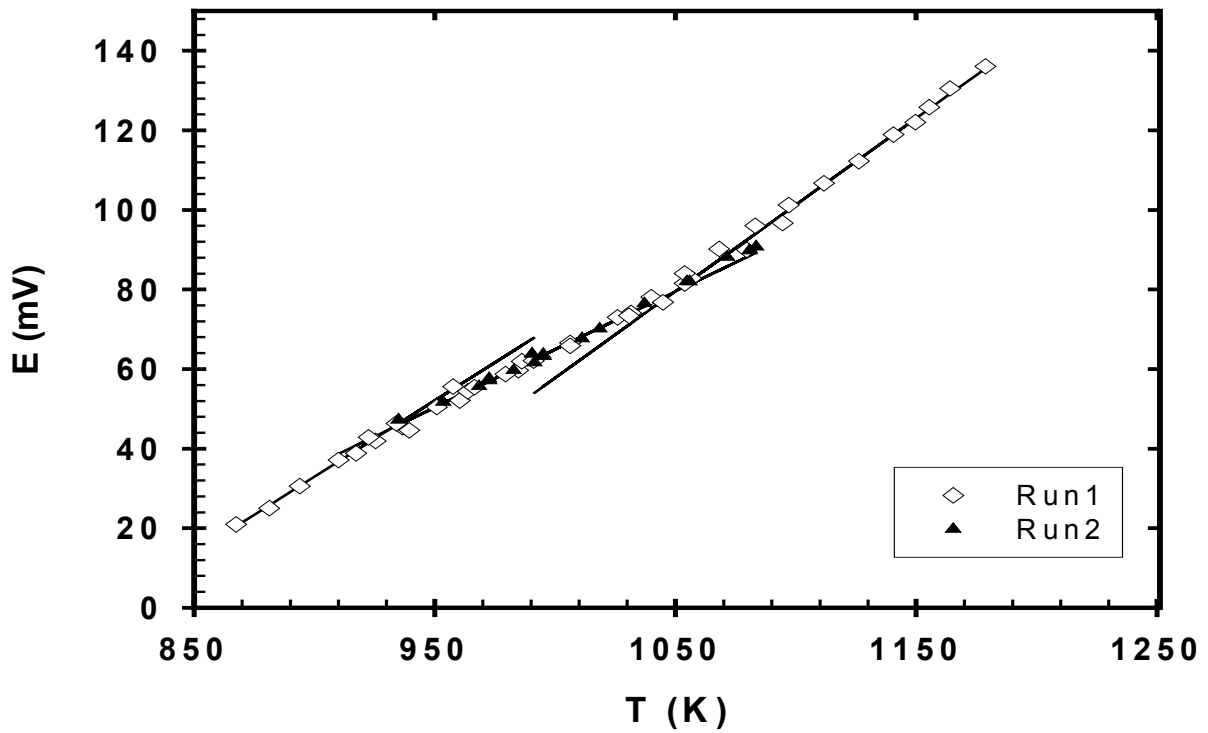

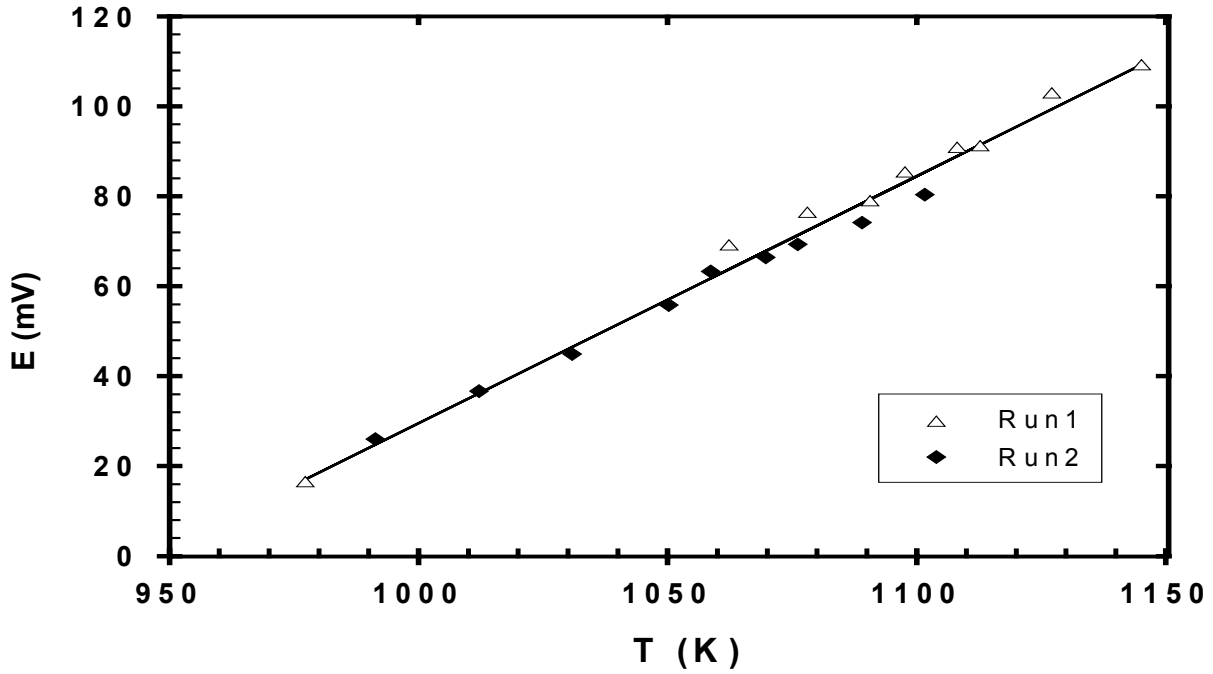**Figue 18. Measured e.m.f. values for Cell II**
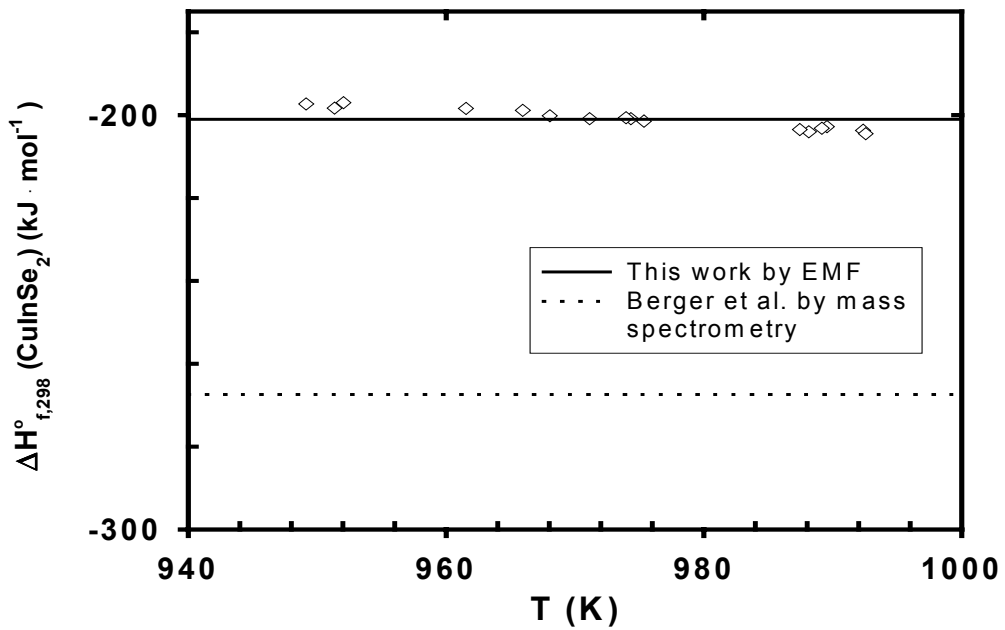
Figure 19. Measured e.m.f. values for Cell III

Fig.4. Third-law treatment of standard enthalpy of formation of $CuInSe_2$ (α)

REFERENCES

[1] Sheng S. Li, B.J. Stanbery, C.H. Huang, C.H. Chang, T.J. Anderson, and Y.S. Chang, *Conf. Record of the 25th PVSC*, 821-824 (1996).

[2] J. Kessler, K.O. Velthaus, M. Ruckh, R. Laichinger, and H.W. Schock, *Proc. 6th Int. PVSEC*, 1005-1010.

[3] D. Lincot, R. Ortega-Borges, J. Vedel, M. Ruckh, J. Kessler, K.O. Velthaus, D. Hariskos, and H.W. Schock, *Proc. 11th E.C. Photovoltaic Solar Energy Conference*, 870-872 (1992).

[4] T.M. Friedlmeier, D. Braunger, D. Hariskos, M. Kaiser, H.N. Wanka, and H.W. Schock, *Conf. Record of the 25th PVSC*, 845-848 (1996).

[5] R.K. Ahrenkiel, *J. Appl. Phys.*, **59**(1), (1986).

[6] C. Goradia and M. Ghalla Coradia, *Solar Cells*, **16**, 611-630 (1986).

[7] J. Gray and T. Simacek, private communication (1997).

[8] K. Ramanathan, present junction group report (1997).

[9] J.R. Tuttle, D.S. Albin, J.P. Goral and R. Noufi, *Conf. Record of the 21st PVSC,* 748-754 (1990).

[10] M.H. Bode, *J. Appl. Phys.,* **76**, 159-162 (1994).

[11] A. Rockett, F. Abou-Elfotouh, D. Albin, M. Bode, J. Erner, R. Klenk, T. Lommasson, T.W.F. Russell, R.D. Tomlinson, J. Tuttle, L. Stolt, T. Walter and T.M. Peterson, *Thin Solid Films*, 1-11 (1994).

[12] J. Hedstrom, H. Ohlsen, M. Bodegard, A. Kylner, L. Stolt, D. Hariskos, M. Ruckh and H.W. Schock, *Conf. Record of the 23rd PVSC,* 364 (1993).

[13] M. Bodegard, J. Hedstrom, K. Granath, A. Rockett and L. Stolt, *Proc. 13th E.C. Photovoltaic Solar Energy Conference,* 2080 (1995).

[14] U. Rau, M. Schmitt, D. Hilburger, F. Engelhardt, O. Seifert and J. Parisi, *Conf. Record of the 25th PVSC*, 1005-1008 (1996).

[15] M. Bodegard, L. Stolt and J. Hedstrom, *Proc. l2th E.C. Photovoltaic Solar Energy Conference,* 1743 (1994).

[16] M. Ruckh, D. Schmid, M. Kaiser, R. Schaffler, T. Walter and H.W. Schock, *Proc. 1st World Conference on Photovoltaic Energy Conversion,* 156, (1994).

[17] J.R. Tuttle, T.A. Berens, J. Keane, K.R. Ramanathan, J. Granata, R.N. Battacharya, H. Wiesner, M.A. Contreras and R. Noufi, *Conf. Record of the 25th PVSC* (1996).

[18] A. Rockett, M. Bodegard, K. Granath and L. Stolt, *Conf. Record of the 25th PVSC,* 985-987 (1996).

[19] H. Oumous, A. Knowles, M.H. Badawi, M.J. Carter and R. Hill, *Proc. 9th E.C. Photovoltaic Solar Energy Conference,* 153 (1989).

[20] A. Knowles, H. Oumous, M.J. Carter and R. Hill, *Conf. Record of the 20th PVSC,* 1482 (1988).

[21] D.S. Albin, G.D. Mooney, A. Duda, J. Tuttle, R. Matson and R. Noufi, *Solar Cells,* **30**, 47-52 (1991).

[22] R. Gay, M. Dietrich, C. Fredric, C. Jensen, K. Knapp, D. Tarrant and D. Willett, *Proc. 12th E.C. Photovoltaic Solar Energy Conference*, 935-938 (1994).

[23] B.M. Basol, V. K. Kapur and A. Halani, *Conf. Record of the 22nd PVSC,* 893-897, (1991).

[24] D.S. Albin, G.D. Mooney, J. Carapella, A. Duda, J. Tuttle, R. Matson and R. Noufi, *Solar Cells*, **30**, 41-46 (1991).

[25] N. Orbey, H. Hichri, R.W. Birkmire and T.W.F. Russell, *Conf. Record of the 25th PVSC,* 981-984 (1996).

[26] R.A. Mickelsen and W.S. Chen, *Appl. Phys. Lett.,* **36**, 371-373 (1980).

[27] W.S. Chen and R.A. Mickelsen, *Proc. Soc. Photo Optical Instrumentation Engineers*, 62 (1981).

[28] E.R. Don, R. Hill and G.J. Russell, *Solar Cells*, **16***,* 131-142 (1986).

[29] D.J. Chakrabarti and D.E. Laughlin, *Bulletin of Alloy Phase Diagrams*, **2**, 305 (1981).

[30] B.J. Stanbery, W.S. Chen, W.E. Devaney and J.M. Stewart, Phase I Annual Subcontract Report No. Contract ZH-1-19019-6 (1992).

[31] J.R. Tuttle, M. Contreras, A. Tennant, D. Albin and R. Noufi, *Conf. Record of the 23rd PVSC*, 415-421 (1993).

[32] M.H. Bode, M.M. Al-Jassim, K.M. Jones, R. Ratson and F. Hasoon, *AIP Conference Proceedings 268: Photovoltaic Advanced Research and Development Review Meeting*, 140-148 (1992).

[33] A.M. Gabor, J.R. Tuttle, D.S. Albin, M.A. Contreras, R. Noufi and A.M. Hermann, *Appl. Phys. Lett.*, 65, 198-200 (1994).

[34] A.M. Gabor, J.R. Tuttle, M. Contreras, D.S. Albin, A. Franz, D.W. Niles and R. Noufi, *Proc. 12th E.C. Photovoltaic Solar Energy Conference*, 939-943 (1994).

[35] F. Karg, V. Probst, H. Harms, J. Rimmasch, W. Riedl, J. Kotschy, J. Holz, R. Treichler, O. Eibl, A. Mitwalsky and A. Kiendl, *Conf. Record of the 23rd PVSC*, 441-446 (1993).

[36] C.H. Chang, A. Davydov, B.J. Stanbery and T.J. Anderson, *Conf. Record of the 25th PVSC*, 849-852 (1996).

[37] J.-Y Emery, L. Brahim-Ostmane, C. Herlemann and A. Cheny, *J. Appl. Phys.,* 3256 (1992).

[38] C. Chatillon and J.-Y Emery, *J. Crystal Growth*, 312-320 (1993).

[39] D.A. Cammack, K. Shahzad and T. Marshall, *Appl. Phys. Lett.*, **56***,* 845-847 (1990).

[40] Z.Z. Kish, V.B. Lazarev, E. Y. Peresh, E.E. Semrad and I.S. Shaplygin, *Russ. J. Inorg. Chem.*, **30***,* 854-856 (1985).

[41] H. Neumann, U.-C. Boehnke, G. Nolze, B. Schumann and G. Kuhn, *J. Alloys and Compounds*, L11-12 (1994).

[42] D. Schmid, M. Ruckh, F. Grunwald and H.W. Schock, *J. Appl. Phys.,* **73**, 2902-2909 (1992).

[43] C. Rincon and S.M. Wasim, *Proc. 7th Int. Conf. on Ternary and Multinary Compounds,* 443-452 (1986).

[44] C. Heske, R. Fink, E. Umback, W. Riedl and F. Karg, *Appl. Phys. Lett.*, **68**, 431-3433 (1996).

[45] L.S. Palatnik and E.J. Rogacheva, Sov. Phys. Dokl., **12**, 503, (1967).

[46] T.I. Koneshova, A.A. Babitsyna and V.T. Kalinnikov, Inorg. Mat. **9**, 18, 1267 (1983).

[47] K.J. Bachmann, M.L. Fearheiley, Y.H. Shing and N. Tran, Appl. Phys. Lett., **44** 407 (1984).

[48] J.C.W. Folmer, J.A. Turner, R. Noufi and D. Cahen, J. Electrochem. Soc., **132** (6), 1319 (1985).

[49] M.L. Fearheiley, Solar Cells, **16**, 91 (1986).

[50] U.C. Boehnke and G. Kuhn, J. Mater. Sci., **22**, 1635 (1987).

[51] K.J. Bachmann, H. Goslowsky, and S. Fiechter, J. Cryst. Growth, **89**, 160 (1988).

[52] M.Y. Rigan, V.I. Tkachenko, N.P. Stasyuk and L.G. Novikova, Inorg. Mat., 304 (1991).

[53] M.F. Zargarova, P.K. Babaeva, D.S. Azhdarova, Z.D. Mekhtieva and S.A. Mekhtieva, Inorg. Mat., **32**, 282 (1995).

[54] S.H. Wei, L.G. Ferreira and A. Zunger, Phys. Rev., **45**(5), 2533 (1992).

[55] I.V. Bodnar and B.V. Korzun, Mat. Res. Bull., **18**, 519 (1983).

[56] L.A. Mechkovski, S.A. Alfer, I.V. Bodnar,and A.P. Bologa, Thermochimica Acta, **93**, 729 (1985).

[57] K.D. Becker and S. Wagner, Phys. Rev. B, **27**(a), 5240 (1983).

[58] L. Garbato, F. Ledda and A. Rucci, Prog. Crystal Growth and Charact., **15**, 1 (1987).

[59] L. I. Berger, S.A. Bondar, V.V. Lebedev, A.D. Molodyk and S.S. Strel'chenko, The Chemical Bond in Crystals of Semiconductors and Semimetals, Nauka I Tekhnika, 248 (1973).

[60] V.M. Glazov, V.V. Lebedev, A.D. Molkyn and A.S. Pashinkin, Inorg. Mat. **15**, 1865 (1979).

[61] J.C. Phillips and J.A. Van Vechten, Phys. Rev., B2, 2147 (1970).

[62] E. Gombia, F. Leccabue and C. Pelosi, Mater. Lett., **2**, 429 (1984).

[63] H. Neumann, Crystal Res. Technol., **18**, 665 (1983).

[64] K.J. Bachmann, F.S.L. Hsu, F.A. Thiel and H.M. Kasper, J. Electron. Mater., **6**, 431 (1977).

[65] H. Neumann, Solar Cells, **16**, 399 (1986).

[66] R.H. Lamoreaux, K.H. Lau and R.D. Brittain, Final Report, SERI Subcontract XZ-2-02001,1983; J.B. Mooney and R.H. Lamoreaux, Solar Cells, **16**, 211 (1986).

[67] D. Cahen and Y. Mirovsky, J. Phys. Chem., **89**, 2818 (1985).

[68] L.M. Khriplovich, I.E. Paukov, W. Moller and Kuhn, Russ. J. Phys. Chem., **58**, 619 (1984).

[69] S.H. Wei, Private Communication.

[70] T. J. Anderson, and L.F. Donaghey, J. Chem. Therm., **9**, 603 (1977).

[71] T.J. Anderson, T.L. Aselage and L.F. Donaghey, J. Chem. Therm., **15**, 927 (1983).

[72] L. Shay and J.H. Wernick, Ternary Chalcopyrite Semiconductors, Pergamon, Oxford (1975).

[73] Mills, Thermodynamic Data for Inorganic Sulphides, Selenides and Tellurides, Butterworths, London (1974).

[74] G.P. Vassilev, B. Daouchi, M.C. Record and J.C. Tedenac, (1997), Private Communication.

[75] D. Cahen and R. Noufi, J. Phys. Chem. Solids, **52**, 947 (1991).

COMMUNICATIONS

Publications

[1] S.S. Li, B.J. Stanbery, C.H. Huang, C.-H.Chang, Y.S. Chang and T.J. Anderson, "Effects of Buffer Layer Processing on CIGS Excess Carrier Lifetime: Application of Dual-beam Optical Modulation to Process Analysis" *Record of the 25th IEEE Photovoltaic Specialist Conference*, 821-824, Washington, DC (1996).

[2] A. Davydov, B.J. Stanbery, T.J. Anderson, "Thermodynamic Assessment of the Cu-In-Se System and Application to Thin Film Photovoltaics" *25th IEEE Photovoltaic Specialist Conference*, 849-852 (1996).

[3] B.J. Stanbery, A. Davydov, C.-H. Chang, T.J. Anderson, "Reaction Engineering and Precursor Film Deposition for CIS Synthesis" *AIP Conference Proceedings* **394**, 579-588 (1997).

[4] B.J. Stanbery, C.-H. Chang, T.J. Anderson, "Engineered Phase Inhomogeneity for CIS Device Optimization" *Inst. Phys. Conf. Ser.* **152**, 915-922, ICTMC-11 (1997).

[5] C.H. Huang, S.S. Li, B.J. Stanbery, C.-H. Huang, T.J. Anderson , "Investigation of Buffer Layer Processes on CIS Solar Cells by Dual Beam Optical Modulation Technique" *Conference Record of the 26th IEEE Photovoltaic Specialist Conference*, 407-410 (1997).

Presentations

[1] Albert Davydov and T.J. Anderson , "Assessment of Thermochemical and Phase Diagram Data for Selected Compound Semiconductors" *212th ACS National Meeting*, Orlando, FL (1996).

[2] C. Mallika, A. Davydov, T.J. Anderson, "Phase Equilibria and Thermochemistry of the In-Se System" *126th TMS Annual Meeting*, Orlando, FL (1997).

[3] C. McCreary, B.J. Stanbery, A. Morrone, A. Davydov, T.J. Anderson, "Growth and Characterization of CdS Thin Films by Chemical Bath Deposition and Metalorganic Chemical Vapor Deposition" *25th Annual Symposium Applied Vacuum Science and Technology*, AVS, Orlando, FL (1997).

[4] A. Davydov, B.J. Stanbery and T.J. Anderson, "Thermodynamic Assessment of Selenium Unary System" *CALPHAD XXVI*, Palm Coast, FL (1997).

[5] B.J. Stanbery, C.-H. Chang and T.J. Anderson, "Engineered Phase Inhomogeneity for CIS Device Optimization" Invited presentation at 11th Int. Conf. on Ternary and Multinary Compounds (ICTMC-11), Salford, UK (1997).

[6] B.J. Stanbery, A. Davydov, C.H. Chang and T.J. Anderson, "Reaction Engineering and Precursor Film Deposition for CIS Synthesis" Presented at the PVPR Meeting, Lakewood, CO (1996).

[7] C.H. Huang, A. Davydov, B.J. Stanbery and T.J. Anderson, "Thermodynamic Assessment of the Cu-In-Se System and Application to Thin Film Photovoltaics" Presented at the 25th IEEE Photovoltaic Specialists Conf., Washington DC (1996).

[8] B.J. Stanbery, E.S. Lambers and T.J. Anderson, "XPS Studies of Sodium Compound Formation and Surface Segregation in CIGS Thin Films" Presented at the 26th IEEE Photovoltaic Specialists Conf., Anaheim, CA (1997).

[9] S. Li, C.-H. Huang, B.J. Stanbery, C.H. Chang and T.J. Anderson, "Investigation of Buffer Layer Processes on CIS Solar Cells by Dual Beam Optical Modulation Technique" Presented at the 26th IEEE Photovoltaic Specialists Conf., Anaheim, CA (1997).

REPORT DOCUMENTATION PAGE

Public reporting burden for this collection of information is estimated to average 1 hour per response, including the time for reviewing instructions, searching existing data sources, gathering and maintaining the data needed, and completing and reviewing the collection of information. Send comments regarding this burden estimate or any other aspect of this collection of information, including suggestions for reducing this burden, to Washington Headquarters Services, Directorate for Information Operations and Reports, 1215 Jefferson Davis Highway, Suite 1204, Arlington, VA 22202-4302, and to the Office of Management and Budget, Paperwork Reduction Project (0704-0188), Washington, DC 20503.

1. AGENCY USE ONLY (Leave blank)	2. REPORT DATE October 1999	3. REPORT TYPE AND DATES COVERED Phase II Annual Report, 6 May 1996 – 5 May 1997

4. TITLE AND SUBTITLE

Processing of $CuInSe_2$-Based Solar Cells: Characterization of Deposition Processes in Terms of Chemical Reaction Analyses; Phase II Annual Report, 6 May 1996 – 5 May 1997

5. FUNDING NUMBERS

C: XAF-5-14142-10
TA: PV005001

6. AUTHOR(S)

Tim Anderson

7. PERFORMING ORGANIZATION NAME(S) AND ADDRESS(ES)

Dept. of Chemical Engineering
University of Florida
Gainesville, FL 32611

8. PERFORMING ORGANIZATION REPORT NUMBER

9. SPONSORING/MONITORING AGENCY NAME(S) AND ADDRESS(ES)

National Renewable Energy Laboratory
1617 Cole Blvd.
Golden, CO 80401-3393

10. SPONSORING/MONITORING AGENCY REPORT NUMBER

SR-520-27296

11. SUPPLEMENTARY NOTES

NREL Technical Monitor: B. von Roedern

12a. DISTRIBUTION/AVAILABILITY STATEMENT

National Technical Information Service
U.S. Department of Commerce
5285 Port Royal Road
Springfield, VA 22161

12b. DISTRIBUTION CODE

13. ABSTRACT *(Maximum 200 words)*

This report describes research performed by the University of Florida during Phase II of this subcontract. First, to study CIGS, researchers adapted a contactless, nondestructive technique previously developed for measuring photogenerated excess carrier lifetimes in SOI wafers. This dual-beam optical modulation (DBOM) technique was used to investigate the differences between three alternative methods of depositing CdS (conventional chemical-bath deposition [CBD], metal-organic chemical vapor deposition [MOCVD], and sputtering). Second, a critical assessment of the Cu-In-Se thermochemical and phase diagram data using standard CALPHAD procedures is being performed. The outcome of this research will produce useful information on equilibrium vapor compositions (required annealing ambients, Se_x fluxes from effusion cells), phase diagrams (conditions for melt-assisted growth), chemical potentials (driving forces for diffusion and chemical reactions), and consistent solution models (extents of solid solutions and extending phase diagrams). Third, an integrated facility to fabricate CIS PV devices was established that includes migration-enhanced epitaxy (MEE) for deposition of CIS, a rapid thermal processing furnace for absorber film formation, sputtering of ZnO, CBD or MOCVD of CdS, metallization, and pattern definition.

14. SUBJECT TERMS

photovoltaics ; $CuInSe_2$; deposition processes ; chemical bath deposition ; buffer-layer processing ; thermochemistry ; phase equilibria ; device processing

15. NUMBER OF PAGES

16. PRICE CODE

17. SECURITY CLASSIFICATION OF REPORT Unclassified	18. SECURITY CLASSIFICATION OF THIS PAGE Unclassified	19. SECURITY CLASSIFICATION OF ABSTRACT Unclassified	20. LIMITATION OF ABSTRACT UL